Cell

A transmitochondrial sodium gradient controls membrane potential in mammalian mitochondria

Graphical abstract

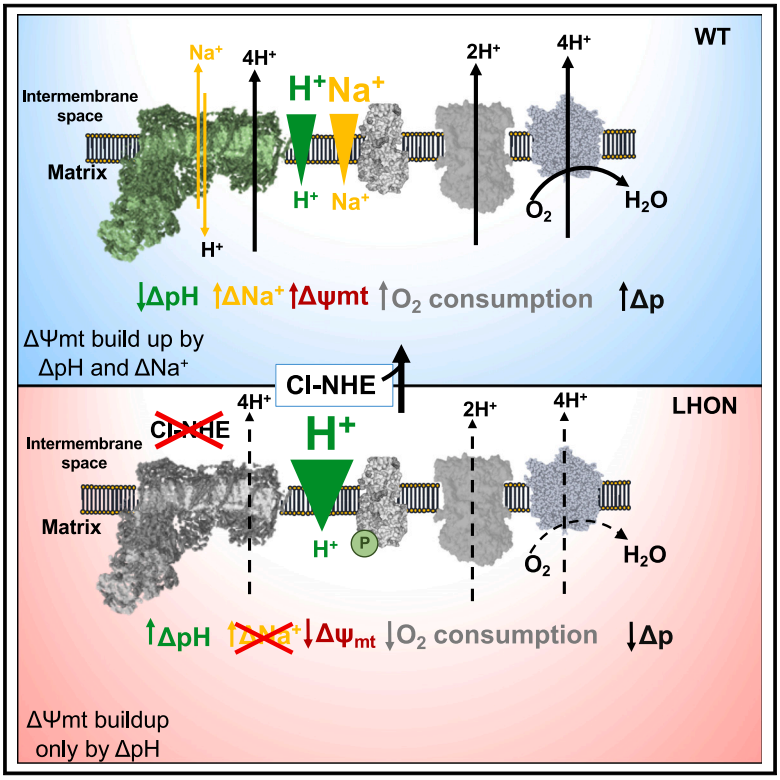

Highlights

- Mitochondrial membrane potential is controlled by a H^+ and a Na^+ gradient
- P-module of CI is the mitochondrial Na^+-specific Na^+/H^+ exchanger (mNHE)
- Mutations in different CI modules produce different bioenergetic phenotypes
- Reduced mNHE function underlines the pathogenesis of the LHON mutation

Authors

Pablo Hernansanz-Agustín, Carmen Morales-Vidal, Enrique Calvo, ..., Iván López-Montero, Jesús Vázquez, José Antonio Enríquez

Correspondence

phernansanz@cnic.es (P.H.-A.), jaenriquez@cnic.es (J.A.E.)

In brief

The mitochondrial complex I functions as a Na^+/H^+ exchanger (mNHE), utilizing the H^+ gradient to build a Na^+ gradient and contribute significantly to the regulation of the mitochondrial membrane potential ($\Delta\Psi$mt).

Hernansanz-Agustín et al., 2024, Cell *187*, 6599–6613
November 14, 2024
https://doi.org/10.1016/j.cell.2024.08.045

CellPress

Cell

CellPress
OPEN ACCESS

Article

A transmitochondrial sodium gradient controls membrane potential in mammalian mitochondria

Pablo Hernansanz-Agustín,[1,2,8,*] Carmen Morales-Vidal,[1] Enrique Calvo,[1,3] Paolo Natale,[4,5] Yolanda Martí-Mateos,[1] Sara Natalia Jaroszewicz,[1] José Luis Cabrera-Alarcón,[1] Rebeca Acín-Pérez,[7] Iván López-Montero,[4,5,6] Jesús Vázquez,[1,3] and José Antonio Enríquez[1,2,9,*]

[1]Centro Nacional de Investigaciones Cardiovasculares Carlos III (CNIC), Madrid 28029, Spain
[2]Centro de Investigación Biomédica en Red de Fragilidad y Envejecimiento Saludable, Madrid, Spain
[3]Centro de Investigación Biomédica en Red de Enfermedades Cardiovasculares (CIBER-CV), Madrid, Spain
[4]Departamento de Química-Física, Facultad de Ciencias Químicas, Universidad Complutense de Madrid (UCM), Madrid, Spain
[5]Instituto de Investigación Biomédica Hospital Doce de Octubre (imas12), Madrid, Spain
[6]Instituto Pluridisciplinar-UCM, Madrid, Spain
[7]Department of Medicine, Endocrinology, David Geffen School of Medicine, UCLA, Los Angeles, CA 90095, USA
[8]Present address: Instituto Cajal, Consejo Superior de Investigaciones Científicas (CSIC), Madrid 28002, Spain
[9]Lead contact
*Correspondence: phernansanz@cnic.es (P.H.-A.), jaenriquez@cnic.es (J.A.E.)
https://doi.org/10.1016/j.cell.2024.08.045

SUMMARY

Eukaryotic cell function and survival rely on the use of a mitochondrial H^+ electrochemical gradient (Δp), which is composed of an inner mitochondrial membrane (IMM) potential ($\Delta\Psi mt$) and a pH gradient (ΔpH). So far, $\Delta\Psi mt$ has been assumed to be composed exclusively of H^+. Here, using a rainbow of mitochondrial and nuclear genetic models, we have discovered that a Na^+ gradient equates with the H^+ gradient and controls half of $\Delta\Psi mt$ in coupled-respiring mammalian mitochondria. This parallelism is controlled by the activity of the long-sought Na^+-specific Na^+/H^+ exchanger (mNHE), which we have identified as the P-module of complex I (CI). Deregulation of this mNHE function, without affecting the canonical enzymatic activity or the assembly of CI, occurs in Leber's hereditary optic neuropathy (LHON), which has profound consequences in $\Delta\Psi mt$ and mitochondrial Ca^{2+} homeostasis and explains the previously unknown molecular pathogenesis of this neurodegenerative disease.

INTRODUCTION

All organisms rely on the formation of transmembrane potentials to support energy balance, and the maintenance/regulation of these transmembrane potentials are crucial determinants of cell homeostasis. Eukaryotes rely on a plasma membrane potential and a mitochondrial inner membrane potential ($\Delta\Psi mt$), the latter being critical for energy production and cell fate determination. The mitochondrial electron transport chain (mETC) is responsible for maintaining $\Delta\Psi mt$ through the function of several complexes and supercomplexes.[1] Mitochondrial complexes I (CI) and II (CII), respectively, oxidize NADH (reduced nicotine adenine dinucleotide) and succinate to reduce ubiquinone (CoQ) to ubiquinol. Complex III (CIII) uses ubiquinol to reduce cytochrome c (cyt c), and complex IV (CIV) oxidizes cyt c to reduce O_2 to H_2O. These series of reactions are coupled to the translocation of H^+ by CI, CIII, and CIV across the inner mitochondrial membrane (IMM), from the matrix to the intermembrane space (IMS), to form a H^+-motive force (Δp). Δp, in turn, activates the phosphorylation of adenosine diphosphate (ADP) to adenosine triphosphate (ATP), which is coupled to the electrophoretic entry of H^+ back to the matrix through a fifth complex (CV). Δp combines an electrical component, $\Delta\Psi mt$, which is negative in the mitochondrial matrix, and a chemical component, ΔpH, which is alkaline in the matrix and acidic in the IMS,[2] with $\Delta\Psi mt$ accounting for approximately 80% of the total Δp.[3] CI is constituted by three structural modules.[4–6] The N-module mediates NADH oxidation and transfers the electrons to the Q-module, also called the CoQ-reducing module. The energy released by the NADH-CoQ oxidoreduction is transferred to the subunits in the H^+ pumping module, or P-module. The P-module contain the mitochondrial DNA (mtDNA)-encoded subunits, which are evolutionarily related to the Na^+/H^+ antiporters of alkaliphilic and halophilic bacteria[7] (Figure 1A).

Mitochondria also contain a panoply of exchangers and antiporters that allow them to maintain respiration, osmolarity, and volume, permit the entry and extrusion of substrates and metabolites, and regulate allosterically many enzymes and transporters.[8] The mitochondrial Ca^{2+} uniporter (MCU) introduces Ca^{2+} into the mitochondrial matrix, which, in turn, is extruded by the mitochondrial Na^+/Ca^{2+} exchanger (NCLX) in an electrogenic exchange for 3 Na^+ ions.[9] Intramitochondrial

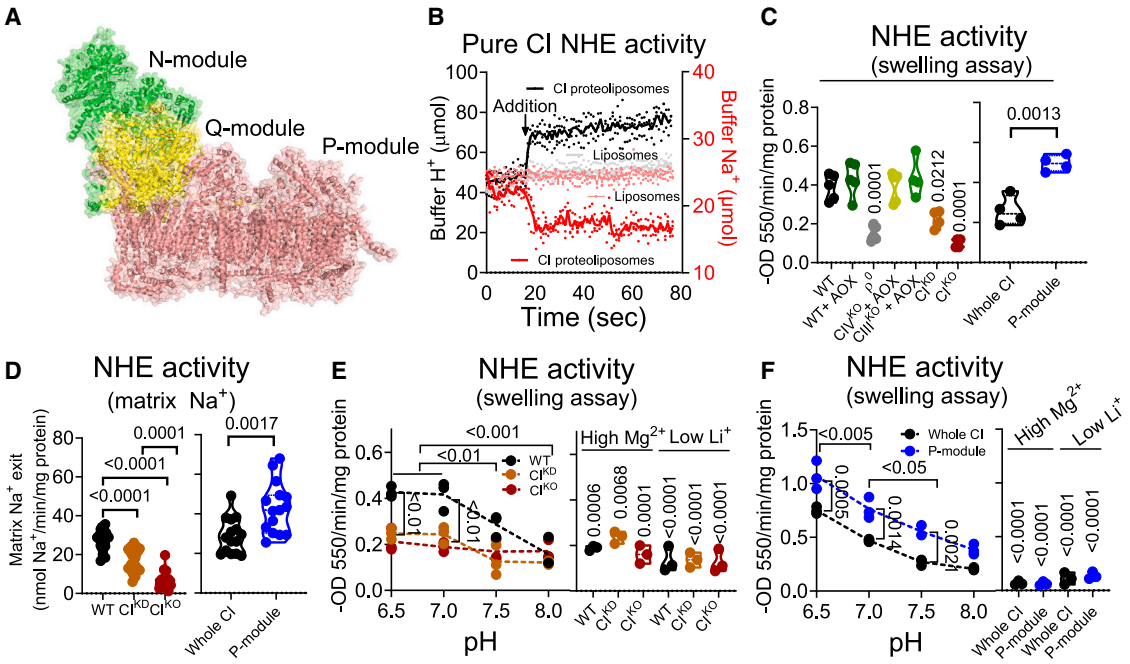

Figure 1. CI is the Na^+-specific mitochondrial NHE

(A and B) (A) Scheme showing CI (B) to forward NHE estimation: buffer pH (left axis) or buffer Na^+ (right axis) content in 1 mL before and after the addition of liposomes (gray or pink) or pure CI-containing proteoliposomes (black or red). CI substrates were not added (n = 3). Each experiment is represented by dotted lines and the mean by a continuous line.

(C) Reverse NHE activity estimation by passive swelling in WT, WT+AOX, ρ^0 (CI, CIII, and CIV absent), CIV^{KO}+AOX (only CIV absent), $CIII^{KO}$+AOX (only CIII absent), CI^{KD}, CI^{KO}, whole CI, and P-module non-respiring mitochondria (n = 4). Ordinary one-way ANOVA in left panel and t test in right panel, p values against WT are shown.

(D) Passive forward NHE activity was measured as a readout of mitochondrial Na^+ exit in WT, CI^{KD}, CI^{KO}, whole CI, and P-module (n = 15; n = 13 in CI^{KO}). p values represent ordinary one-way ANOVA in left panel and t test in right panel.

(E) Passive swelling reverse NHE activity in WT, CI^{KD}, and CI^{KO} was assessed in different buffer pHs and in the presence of 50 mM $MgCl_2$ or with 2 mM LiCl (n = 3). p values represent two-way ANOVA comparing all conditions in the assay.

(F) Passive swelling reverse NHE activity in whole CI and P-module was assessed in different buffer pHs and in the presence of 50 mM $MgCl_2$ or with 2 mM LiCl (n = 3). p values represent two-way ANOVA comparing all conditions in the assay.

(E and F) p values in high Mg^{2+} and low Li^+ are against WT or whole CI at their corresponding, same pH (i.e., pH 7).

Violin plots in this figure show dots representing every replicate and a dotted line indicating the mean of all experiments.

See Figures S1 and S2.

Na^+ exit is mediated by an unknown electroneutral Na^+/H^+ exchanger, which extrudes Na^+ to the IMS and enters H^+ into the matrix, acidifying it.[10] Classically, there have been two NHE functions ascribed to mitochondria: (1) a highly active, Na^+-specific NHE, inhibitable by "low Li^+," "high Mg^{2+}," and alkaline pH (mNHE henceforth) and (2) a sluggish Na^+-unspecific (i.e., it also catalyzes K^+/H^+ antiport) NHE, inhibitable by low Mg^{2+} and acidic pH (K^+/H^+ exchanger [KHE] henceforth).[11–17]

In 2004, based on sequence similarity with alkalophilic bacterial Na^+/H^+ antiporters,[7] Stolpe and Friedrich reconstituted purified CI from *E. coli* into liposomes and proposed that prokaryotic CI may be capable of a secondary Na^+ antiport activity (that may occur in coordination with NADH:CoQ oxidoreduction and H^+ pumping),[18] which was confirmed by Pereira's group.[19] Later, it was suggested that bovine CI, only in its deactive form, could behave as a Na^+/H^+ antiporter (Na^+/H^+ antiport occurs only when the enzyme is catalytically inactive).[20] These *in vitro* approaches suggested the possibility of CI being a Na^+/H^+ exchanger. However, the type of antiporter (mNHE or KHE) and whether it functioned under physiological conditions were neither proposed nor proven.

In this work, by reconstituting CI into proteoliposomes and using a panoply of mETC mutants, we show that the long-sought mNHE is the P-module of CI. Most importantly, by applying a multiplexed approach to six different CI-deficiency models, we demonstrate that mammalian mitochondria possess a Na^+ gradient parallel to the H^+ gradient, which is reliant on the CI-dependent mNHE function. The electrical contribution of the Na^+ gradient accounts for half of the $\Delta\Psi$mt in coupled-respiring mitochondria. We also found that the mNHE activity of CI is compromised in the most common mutation causing Leber's hereditary optic neuropathy (LHON), which does neither affect CI assembly nor its enzymatic activity but shows profound alterations in respiration, $\Delta\Psi$mt, and cation homeostasis. Thus, we propose an update for the current bioenergetic model in which only a H^+ gradient governs energy conversion. In the new model,

the H^+ gradient is paralleled by a Na^+ gradient working as a $\Delta\Psi$mt reservoir, which can be regulated by assembly or conformational changes of CI.

RESULTS

Respiratory CI is the mitochondrial Na^+-specific Na^+/H^+ antiporter

To evaluate the possibility of eukaryotic CI being a Na^+/H^+ antiporter, we first purified CI from pig heart mitochondria (Figures S1A–S1D) and reconstituted it into proteoliposomes with its N-module out (Figure S1E). In contrast to liposomes alone, CI proteoliposomes showed a strong Na^+/H^+ exchanger activity (Figures 1B and S1F–S1H). To pinpoint which CI module was exerting such activity, we used CI inhibitors binding to different modules of CI (Figure 1A). The N-module-binding drug diphenyleneiodonium (DPI) did not inhibit Na^+/H^+ antiport nor did a low dose the Q-module-binding drug rotenone (Figure S1I). However, high-dose rotenone and the P-module-binding-inhibitor ethyl-isopropyl amiloride (EIPA) did inhibit CI-dependent Na^+/H^+ antiport (Figure S1I). The apparently discrepant results between low- and high-dose rotenone treatment can be explained by considering that high-dose rotenone displays an alternative binding site at the P-module- protein ND4, as predicted by recent structures,[21,22] acting then as a P-module inhibitor. Thus, these results point to the P-module as the region in CI exerting passive Na^+/H^+ exchange in proteoliposomes, for which CI redox cycling is not required. This would agree with the previous proposal suggestion that a residual Na^+/H^+ antiporter activity could only be observed with the deactive conformation of mammalian CI.[20]

Next, we wondered whether such CI-dependent NHE activity could be measured in intact mitochondria. First, we evaluate in isolated mitochondria the NHE activity when CI was in fully activated or fully deactivated conformation. We found that deactivation was not a requisite for Na^+/H^+ antiport in CI, though it significantly increased the rate of exchange (Figure S1J). Next, to precisely assess if the NHE activity in intact mitochondria was responsibility of CI, we used several cellular knock-out (KO) models of different oxidative phosphorylation (OXPHOS) subunits: (1) a mutant in mitochondrial-encoded CI subunit ND6 with reduced levels of, but still present, CI, named CI knock-down (CI^{KD}),[23] which only shows partial CI assembly by blue-native-polyacrylamide gel electrophoresis (BN-PAGE) (Figure S2A); (2) a ND6 mutant with a complete loss of CI, named CI^{KO}, which shows no detectable CI by BN-PAGE (Figure S2A)[24]; (3) and a knockout (KO) model of the CI nuclear-encoded subunit NDUFS4 or $NDUFS4^{KO}$, which renders the N-module stability within CI severely weakened, leaving the P-module consistently stable by BN-PAGE (named P-module; Figure S2B); (4) a variety of cell lines lacking either all mtDNA-encoded OXPHOS complexes (ρ° cells) or only CIII or CIV.[25]

CI^{KD}, CI^{KO}, and P-module cell lines displayed a significant decrease in NADH dehydrogenase (DH) enzymatic CI activity being proportional to the residual assembled CI (Figures S2A–S2D). However, whereas CI^{KD} and CI^{KO} mitochondria showed a reduction in Na^+/H^+ antiport proportional to their CI content, P-module mitochondria produced a marked increase in it (Figures 1C, 1D, and S2E–S2J). These results indicate that neither CI NADH DH enzymatic activity nor the N-module were required for mitochondrial Na^+/H^+ exchanger (mNHE) function. Importantly, the specific removal of any other mETC complex, while preserving CI, did not affect mitochondrial Na^+/H^+ antiport (Figures 1C). All these indicate that intact mitochondria retain its Na^+/H^+ exchanger function as long as the P-module of CI is present, regardless of the absence of other mETC complexes, supporting the potential physiological implication of the Na^+/H^+ antiporter activity observed in pure CI.

As mentioned above, two types of Na^+/H^+ antiporters have been functionally identified in mammalian mitochondria: a mNHE and a KHE.[11–17] We observed that neither of the CI-deficient cell models displayed a detectable alteration in mitochondrial KHE function (Figures S2K–S2M). Also, the pH-dependency profile showed that a rapid Na^+/H^+ antiporter becomes inhibited with increasing buffer pH only in the presence of CI (Figure 1E) or its P-module (Figure 1F). Finally, Na^+/H^+ antiport activity was inhibited to similar values by high amounts of Mg^{2+} or low levels of Li^+ (Figures 1E and 1F). Altogether, these results indicate that the P-module of mitochondrial CI constitutes the bona fide, Na^+-selective, mNHE.

mNHE differentially affects respiration and $\Delta\Psi$mt in several models of CI deficiency

CI^{KD} and CI^{KO} cells represent partial or total mNHE loss-of-function models, respectively, whereas the P-module cells maintain their mNHE function. Thus, they constitute a useful tool for assessing the role of mNHE activity in bioenergetics. Given that CI activity was lower in all models in comparison to their wild-type (WT) counterparts, we bioenergetically characterized them under CII substrates (i.e., succinate). We found that all cell models showed an increase in combined antimycin A-dependent succinate:cyt c (i.e., CII+III) activity compared with their respective isogenic controls (Figures 2A and S3A, summarized in Table S1). Increased "CII+III activity" is a well-known consequence of CI deficiency or inhibition.[23] In addition, CI^{KO} and P-module, but not CI^{KD}, showed elevated CIV activity (Figures 2B and S3B), while CV activity, in forward or reverse modes, was higher only in P-module mitochondria (Figures S3C and S3D, summarized in Table S1). Of note, CIV and CV are not lower in either model than in their respective WT controls. Since CII is rate limiting for succinate-dependent respiration,[26] it is expected that when fueled with succinate, the increase in CII+III activity in all mutants would be accompanied by a raise in CII-CIII-CIV respiration. By the same token, it is expected that when fueled with succinate, those mitochondria will be hyperpolarized (i.e., due to higher H^+ pumping by CIII and CIV). Surprisingly, only P-module mitochondria accomplished such expectation (Figures 2C–2H and S3E–S3G, summarized in Table S1).

We next inquired if the discrepant effect in the bioenergetic footprint of the different mutant cell lines may be due to differences in their origin or genetic background. The different CI-deficient cell lines analyzed were obtained from two different mouse strains. CI^{KD} and CI^{KO} are cybrids with the nucleus of L929 cells, and $NDUFS4^{WT}$ (labeled as Whole CI) and $NDUFS4^{KO}$ (labeled as P-module) are mouse adult fibroblasts isolated from C57BL/6J

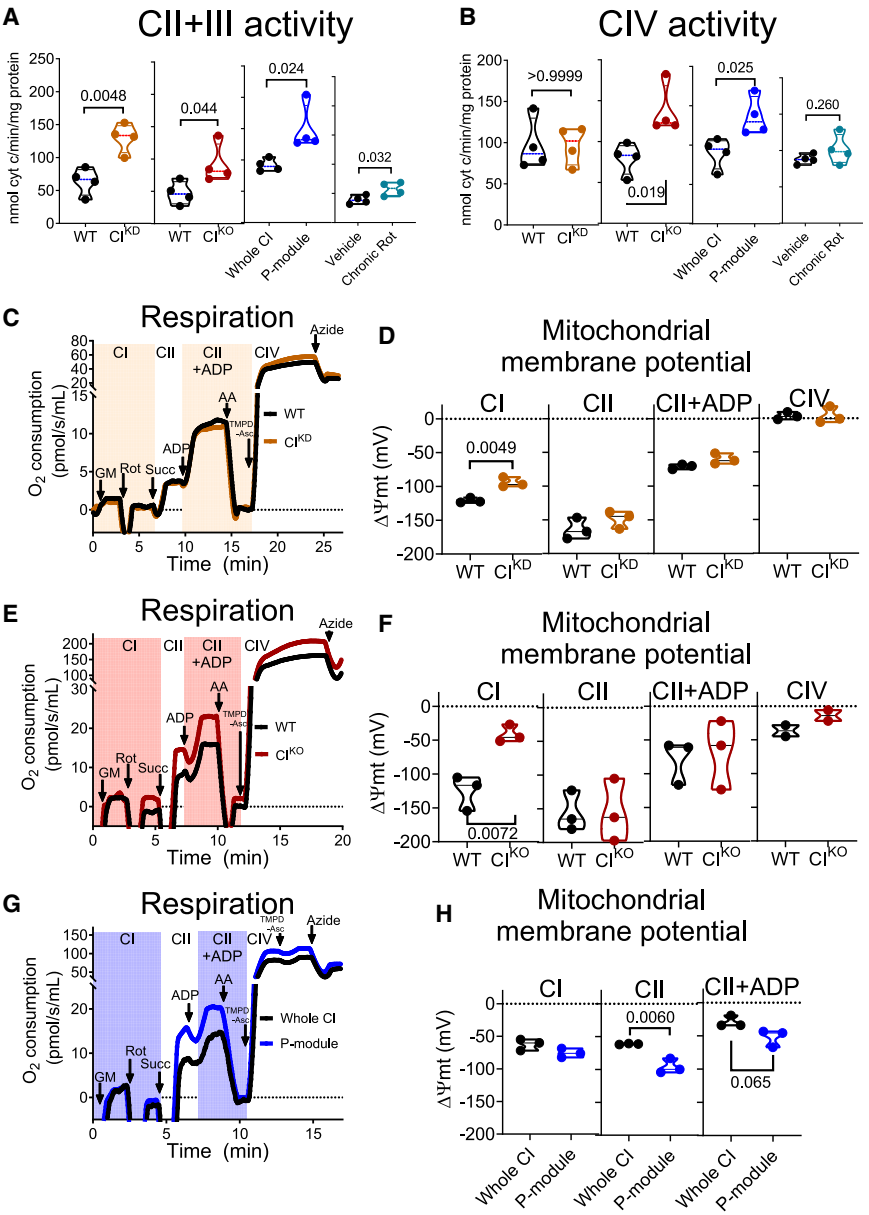

Figure 2. Characterization of CI-deficient models

(A) Antimycin A (AA)-sensitive succinate-cyt c oxidoreductase activity in WT/CI^{KD}, WT/CI^{KO}, whole CI/P-module, and mitochondrial membranes from WT cells treated for 6 h with vehicle or 250 nM rotenone (chronic Rot; n = 4).

(B) Potassium cyanide (KCN)-sensitive cyt c oxidase activity in WT/CI^{KD}, WT/CI^{KO}, whole CI/P-module, and chronic Rot mitochondrial membranes (n = 4).

(C, E, and G) Oxygen consumption rates in WT/CI^{KD} (C, n = 3), WT/CI^{KO} (E, n = 3), and whole CI/P-module isolated mitochondria (G, n = 3). GM, glutamate/malate; Rot, 1 μM rotenone; Succ, succinate; ADP, adenosine di-phosphate; AA, 1 μM antimycin A; TMPD+Asc, N,N,N′,N′-tetramethyl-p-phenylenediamine + ascorbate; azide, 50 mM, sodium azide. CI, CI-dependent respiration; CII, CII-dependent respiration; CII+ADP, CII+ADP-dependent respiration; and CIV, CIV-dependent respiration.

(D, F, and H) Calibrated tetramethylrhodamine methyl ester (TMRM) signal in WT/CI^{KD} (D, n = 3), WT/CI^{KO} (F, n = 3; CIV, n = 2), and whole CI/P-module cells (H, n = 3), providing the CI+III+IV-dependent ΔΨmt (panel CI), CII+III+IV-dependent ΔΨmt (panel CII), CII+CIII+CIV+ADP-dependent ΔΨmt (panel CII+ADP), and CIV-dependent ΔΨmt (panel CIV).

Violin plots in this figure show dots representing every replicate and a dotted line indicating the mean of all experiments. p values in this figure represent t test analysis.

See Figures S3, S4, and S5 and Table S1.

mice. To assess this, we exposed cells with L929 nucleus and WT mtDNA to a chronic, low dose of the CI inhibitor rotenone, leaving CI structurally intact, a treatment known to increase CII activity by phosphorylation of one of its subunits[23]. We measured CII+III, CIV, and CV activities (Figures 2A, 2B, S3C, and S3D) and found an elevation in CII+III activity after rotenone exposure, which translated into an increase in succinate-dependent respiration and hyperpolarization (Figures S3H and S3I, summarized in Table S1). Given that these results resemble that of those in P-module mitochondria, this demonstrates that the observed bioenergetic differences are not due to their origin or genetic background.

Next, we assessed if the bioenergetic differences seen in the CI-deficiency models may be due to phenotypic differences between WT and CI^{KD} and CI^{KO} mitochondria in parameters known to affect bioenergetics, such as mitochondrial volume, ultrastructure, or IMM permeability. We did not observe changes in mitochondrial volume (Figures S4A–S4D), ultrastructure (Figure S4C), fragmentation (Figures S4D and S4E), or IMM permeability (Figures S4F–S4I) that could explain the observed bioenergetic defects.

We next wondered whether the differences between CI^{KD}, CI^{KO}, and P-module mitochondria observed under CII substrates may be due to a succinate-specific effect and whether they could be seen under different substrates. N,N,N,N-tetramethyl-p-phenylenediamine (TMPD)-Asc donate electrons to cyt c and provide a direct readout of respiration and ΔΨmt by CIV, thus avoiding possible effects of substrate import into mitochondria and potential differences in electron flux through other, upstream complexes. Given their differences in isolated CIV activity (Figure 2B), we would expect hyperpolarization in CI^{KO} and P-module mitochondria, but not in CI^{KD}. However, the expectations were again exclusively fulfilled by P-module mitochondria (Figures S4J and S4K). This rules out the possibility of differential substrate management being the cause behind the observed divergent bioenergetics.

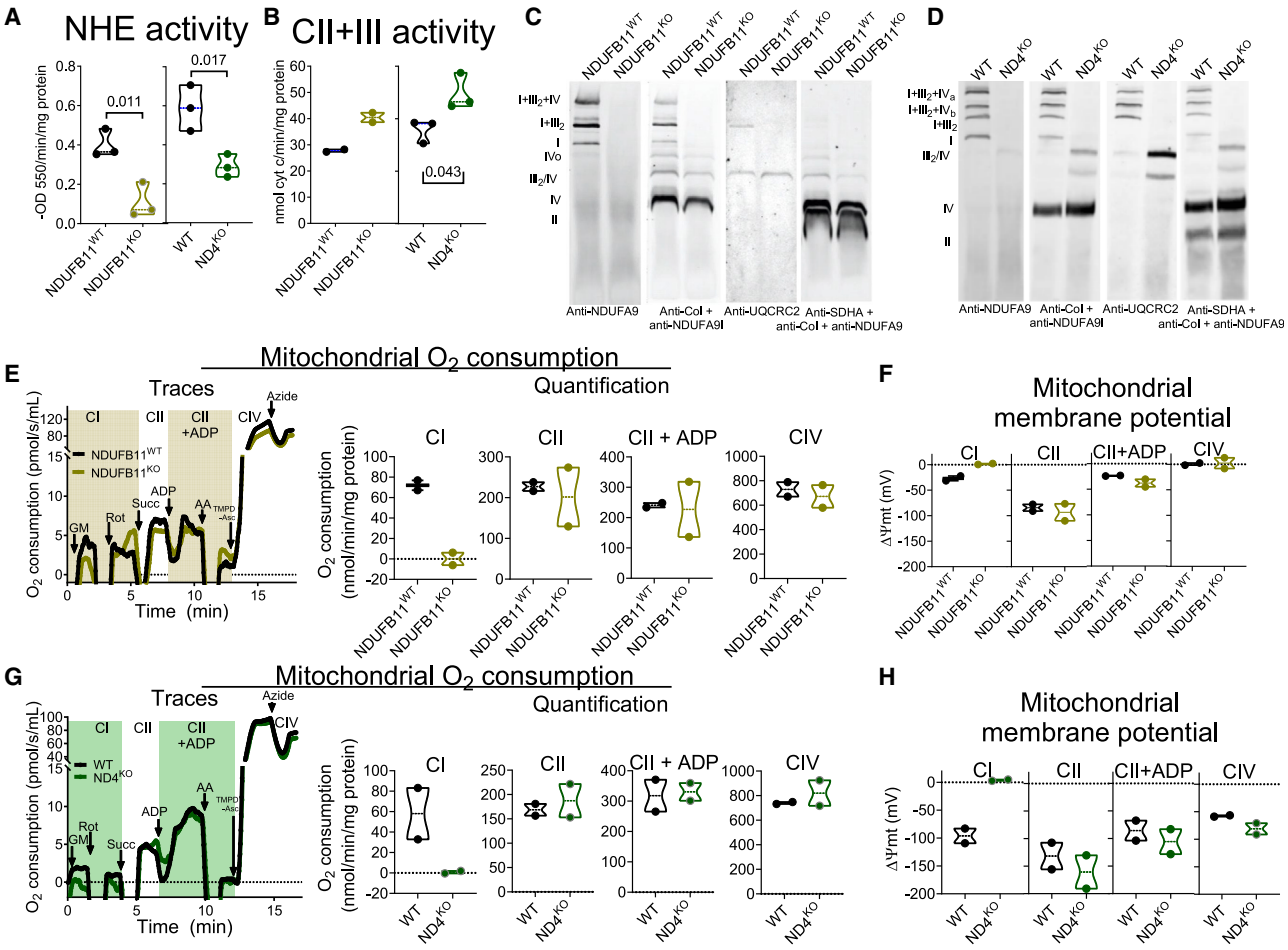

Figure 3. Deletion of a nuclear-encoded or distinct mtDNA-encoded CI subunit in the P-module resembles the bioenergetic footprint of CI^{KD} and CI^{KO}

(A) Passive reverse NHE activity swelling assay in NDUFB11^{WT}, NDUFB11^{KO}, WT, and ND4^{KO} intact mitochondria (n = 3).

(B) Antimycin A (AA)-sensitive succinate-cyt c oxidoreductase activity in NDUFB11^{WT}, NDUFB11^{KO}, WT, and ND4^{KO} mitochondrial membranes (n = 2 in NDUFB11^{KO} and n = 3 in ND4^{KO}).

(C and D) BN-PAGE of mitochondria from NDUFB11^{WT}, NDUFB11^{KO} (C), WT, and ND4^{KO} (D; n = 2) blotted against the same epitopes as in Figure S2A, except for CV. The lateral labels indicate the migrated positions of all detected complexes and supercomplexes.

(E) Oxygen consumption rates were measured in NDUFB11^{WT} and NDUFB11^{KO} isolated mitochondria (n = 2). Insets and acronyms are the same as in Figure 2. Traces are shown in the left, and quantification of respiration is shown in the right.

(F) Calibrated TMRM signal in NDUFB11^{WT} and NDUFB11^{KO} isolated mitochondria (n = 2), respiring on CI substrates (CI inset), CII substrates (CII inset), or CII substrates + ADP (CII+ADP inset).

(G) Oxygen consumption rates were measured in WT and ND4^{KO} isolated mitochondria (n = 2). Insets and acronyms are the same as in Figure 2. Traces are shown in the left, and quantification of every type of respiration is shown in the right.

(H) Calibrated TMRM signal in WT and ND4^{KO} isolated mitochondria (n = 2), respiring on CI substrates (CI inset), CII substrates (CII inset), or CII substrates + ADP (CII+ADP inset).

Violin plots in this figure show dots representing every replicate and a dotted line indicating the mean of all experiments. p values in this figure represent t test analysis.

See also Figure S5.

Finally, the observed effect may be due to the fact that we were comparing mtDNA mutants (CI^{KD} and CI^{KO}) against a KO of a nuclear-encoded CI subunit (P-module). Thus, we studied the bioenergetic footprint and NHE activity comparing a different mtDNA mutant (ND4^{KO}) and a KO of another nuclear-encoded CI subunit (NDUFB11), both affecting the integrity of CI P-module. All parameters measured in NDUFB11^{KO} and ND4^{KO} cells resembled those in CI^{KD} and CI^{KO}: lower NHE activity (Figure 3A), higher CII+III activity (Figure 3B), similar degree of CI loss (Figures 3C and 3H), and equal respiratory and ΔΨmt values than their isogenic counterparts under CII and CIV substrates (Figures 3E–3H). These results demonstrate that the bioenergetic differences between the mitochondria with a complete absence of CI and the ones presenting exclusively the P-module cannot be attributed to the genome

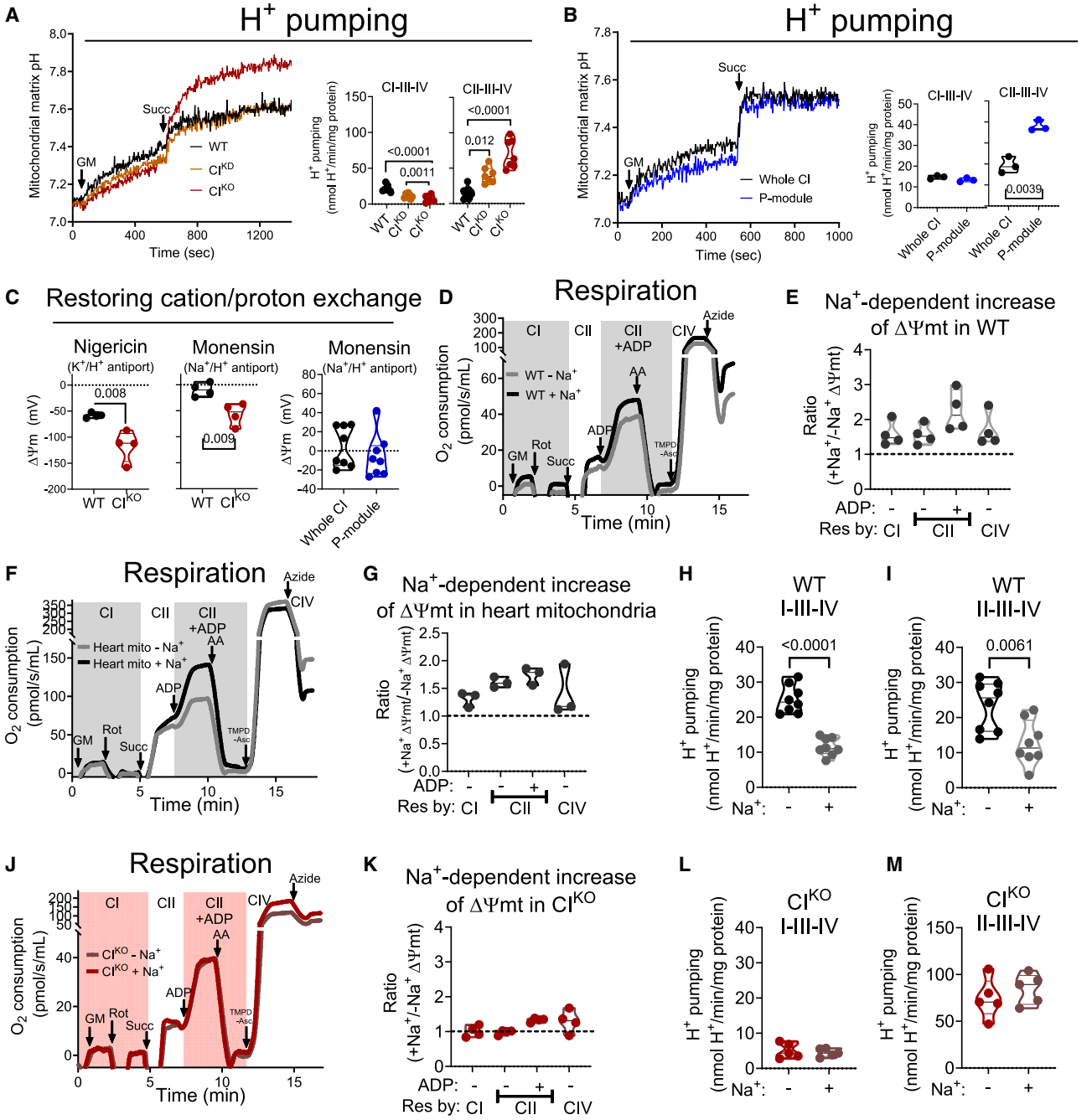

Figure 4. mNHE activity-dependent Na^+ gradient contributes to total $\Delta\Psi$mt

(A) Calibrated BCECF-AM signals of WT, CI^{KD}, and CI^{KO} isolated mitochondria under CI (inset CI-CIII-CIV) and CII substrates (inset CII-CIII-CIV). *p* values in this figure represent ordinary one-way ANOVA analysis.

(B) Calibrated BCECF-AM signals of whole CI and P-module isolated mitochondria under CI (inset CI-CIII-CIV) and CII substrates (inset CII-CIII-CIV). *p* values in this figure represent t test analysis.

(C) Subtraction of calibrated TMRM signal of WT and CI^{KO} mitochondria after and before the addition of nigericin (100 nM) or monensin (100 nM) and only monensin (100 nM) in whole CI and P-module isolated mitochondria respiring in Rot/Succ+ADP. *p* values in this figure represent t test analysis.

(D) Oxygen consumption rates measured in WT in mitochondria in Na^+-containing buffer (black) and Na^+-free buffer (gray; $n = 4$).

(E) Relative contribution of Na^+ to $\Delta\Psi$mt in WT mitochondria respiring on different substrates, calculated as the ratio of the calibrated TMRM signal in Na^+-containing buffer to that in Na^+-free buffer ($n = 4$).

(F) Oxygen consumption rates measured in C57BL/6J heart in mitochondria in Na^+-containing buffer (black) and Na^+-free buffer (gray; $n = 3$).

(G) Relative contribution of Na^+ to $\Delta\Psi$mt in C57BL/6J heart mitochondria respiring on CI, CII, CII+ADP, or CIV substrates, calculated as the ratio of the calibrated TMRM signal in Na^+-containing to that in Na^+-free buffer ($n = 3$).

(legend continued on next page)

(mtDNA or nuclear DNA) that encodes the affected CI subunit, nor to a particular type of mutation.

To complete the characterization of the different cell models, we performed proteomic studies of all cell lines. Principal component analysis of bulk proteomics revealed that the two different WT cell lines grouped together despite their differing genetic background (Figure S5A). In addition, WT cells were well differentiated from all CI mutant cell lines (Figure S5A). Moreover, the CI^{KD} and CI^{KO} cells grouped very close but clearly separated from the proteome of P-module cells (Figure S5A). This was confirmed by gene set enrichment analysis (GSEA), which identified the Gene Ontology pathways that were significantly downregulated (Figure S5B) or upregulated (Figure S5C) in the CI-deficient cells. In both cases, these pathways were very similar between CI^{KD} and CI^{KO} and clearly divergent from those of P-module cells. Finally, proteomic analyses of isolated mitochondria confirmed that CI^{KD} and CI^{KO} had a progressive loss of all CI subunits (Figure S5D), whereas P-module mitochondria retained most of its P-module subunits, showing a significant reduction in N-module and Q-module subunits (Figures S5H and S5L). This confirms that although $NDUFS4^{KO}$ cells can still assemble an almost complete CI,[25] they accumulate CI P-module subassemblies lacking N and Q subunits. No significant differences were observed in other mETC complexes (Figures S5E–S5G and S5I–S5K). Volcano plots show changes found in mitochondria from all cell models; however, we failed to see differences in the presence of the mitochondrial succinate carrier Slc25a10 or other proteins that may affect CII- and CIV-dependent respiration (Figure S5M). In summary, no feature other than the mNHE activity was associated with the divergent bioenergetic signature that is characteristic of the different CI-deficient cell models.

A Na^+ gradient controls respiration and $\Delta\Psi$mt

Comparing the bioenergetic data from all our models, we noticed a correlation between mNHE activity, respiration, and $\Delta\Psi$mt. CI^{KD} and CI^{KO} displayed reduced mNHE activity and could neither increase the respiration nor hyperpolarize under CII or CIV substrates, despite having higher CII+III activity. On the other hand, P-module mitochondria showed an elevated mNHE function and higher respiration and hyperpolarization, correlating well with the fact that they display higher CII+III activity (compare respiration and $\Delta\Psi$mt with mNHE columns in Table S1). As presented by Peter Mitchell in his Nobel lecture,[27] the flux of electrons is coupled to the ejection of H^+ across the IMM. Thus, it was possible that there is a defect in electron transfer or H^+ pumping by CIII and/or CIV in the intact mitochondria of CI^{KD} and CI^{KO}, which precludes them from reaching the respiratory values and hyperpolarization seen in the P-module mitochondria, despite having higher CII+III activity. To assess this question, we measured H^+ pumping directly by measuring mitochondrial matrix pH in the same conditions as the previous experiments. As expected, H^+ pumping was lower in all three models when they were reliant on CI substrates (CI-III-IV inset and traces in Figures 4A and 4B). However, under CII substrates, CI^{KD} and CI^{KO} mitochondria showed higher H^+ pumping than their isogenic control, resembling P-module mitochondria (CII-III-IV inset, traces in Figures 4A and 4B and summarized in Table S1). This finding rules out that H^+ pumping by CIII or CIV is defective in CI^{KD} and CI^{KO} models. Interestingly, it also agrees well with the higher CII+III activity in all CI-deficiency models (compare CII+III activity and "succinate-driven H^+ pumping" columns in Table S1) and further supports that mitochondrial succinate import is not differentially altered in any of the CI-deficiency models. However, a puzzling observation was that despite CI^{KD} and CI^{KO} mitochondria showed higher H^+ pumping (i.e., higher electron transfer), this did not translate into a higher respiration or hyperpolarization.

We then thought that this contradictory observation may be due to the activity of mNHE. It is possible that the lower apparent H^+ pumping in WT, in comparison to CI^{KD} and CI^{KO}, is due to the H^+ dissipating effect of mNHE since its function is to enter $1H^+$ into the mitochondrial matrix and exit $1Na^+$ to the IMS in an electroneutral antiport. Such an exchange would dissipate the H^+ gradient while building up a Na^+ gradient, making the H^+ pumping by WT apparently lower than CI^{KD} and CI^{KO}. This hypothesis implies three main consequences: (1) CI^{KD} and CI^{KO} would be unable to generate a Na^+ gradient, (2) the H^+-dissipating effect of mNHE would increase respiratory rates, and (3) the transmitochondrial Na^+ gradient would contribute to the formation of $\Delta\Psi$mt in respiring mitochondria.

To evaluate this hypothesis, we first recorded $\Delta\Psi$mt in WT and CI^{KO} mitochondria, supplied with CII substrates, and the addition of the chemical Na^+/H^+ exchanger monensin to acutely restore NHE function in isolated mitochondria. Whereas nigericin, a chemical K^+/H^+ exchanger, promoted hyperpolarization in isolated WT mitochondria (left inset in Figure 4C), monensin did not (middle inset in Figure 4C). By contrast, both drugs supported hyperpolarization of CI^{KO} mitochondria (left and middle insets in Figure 4C), indicating that the restoration of a Na^+ gradient by monensin addition contributed to the establishment of $\Delta\Psi$mt in CI^{KO} mitochondria. No similar phenomenon was observed in P-module mitochondria (right inset in Figure 4C).

Second, we reasoned that if a Na^+ gradient contributed to the buildup of $\Delta\Psi$mt, isosmotically removing Na^+ from the respiratory buffer would lead to mitochondrial depolarization and a decrease in respiration in WT mitochondria. Thus, we measured respiratory rates and $\Delta\Psi$mt in intact WT mitochondria maintained in an

(H and I) Mitochondrial matrix H^+ pumping measured from the BCEFC-AM signal in WT isolated mitochondria respiring on CI (H) or CII (I) substrates in Na^+-containing and Na^+-free buffer ($n = 8$). p values in this figure represent t test analysis.
(J) Oxygen consumption rates measured in CI^{KO} mitochondria in Na^+-containing buffer (red) and Na^+-free buffer (brown; $n = 4$).
(K) Relative contribution of Na^+ to $\Delta\Psi$mt in CI^{KO} mitochondria respiring on CI, CII, CII+ADP, or CIV substrates, calculated as the ratio of the calibrated TMRM signal in Na^+-containing to that in Na^+-free buffer ($n = 4$).
(L and M) Mitochondrial matrix H^+ pumping measured from the BCEFC-AM signal in CI^{KO} isolated mitochondria respiring on CI (L) or CII (M) substrates in Na^+-containing and Na^+-free buffer ($n = 5$).
Violin plots in this figure show dots representing every replicate and a dotted line indicating the mean of all experiments.
See Figure S6.

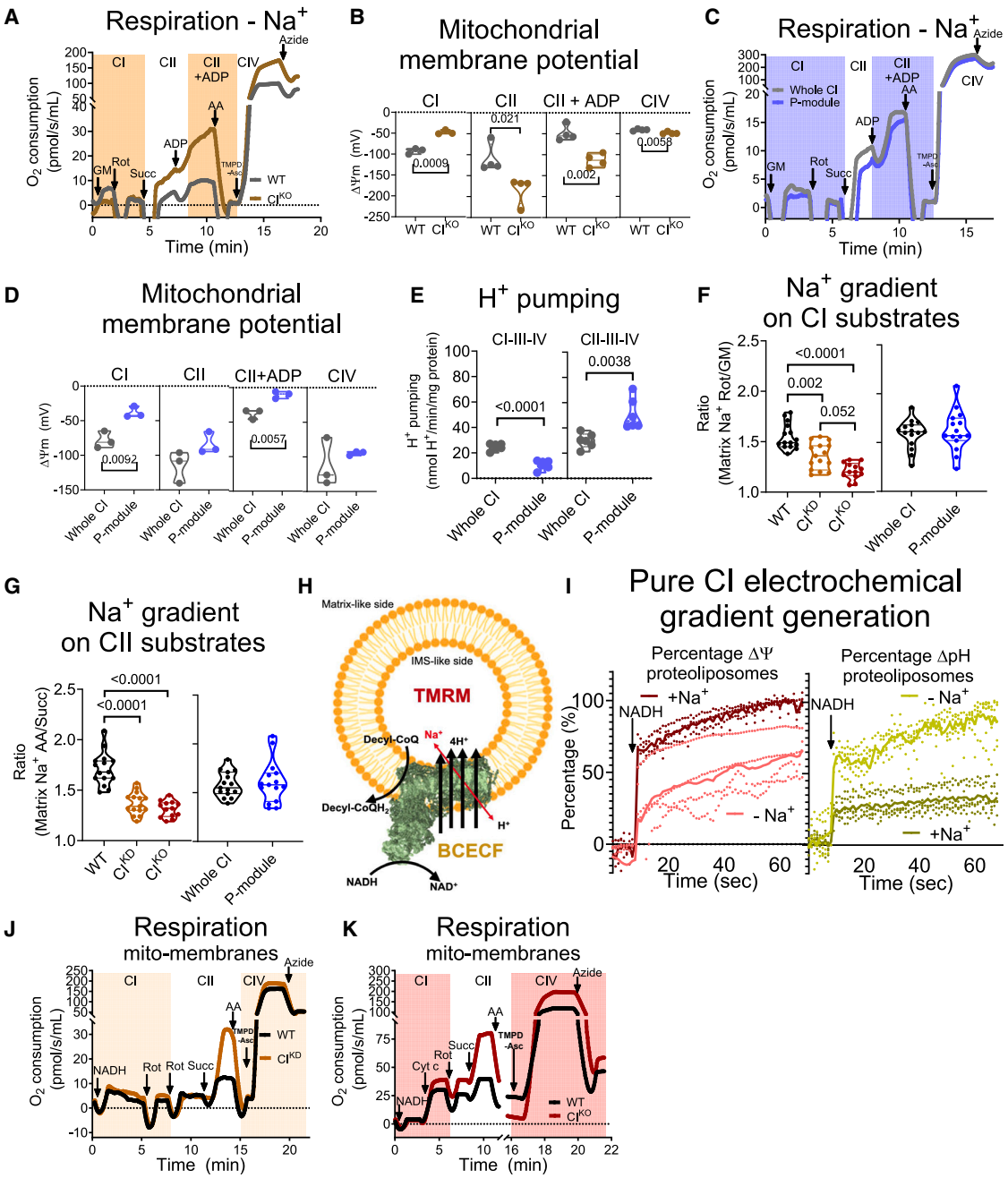

Figure 5. The Na^+ gradient by mNHE increases respiratory and total $\Delta\Psi$mt values

(A) Oxygen consumption rates measured in WT and CI^{KO} mitochondria in Na^+-free buffer (n = 4).

(B) Calibrated TMRM signal in WT and CI^{KO} mitochondria respiring on CI substrates (CI inset), CII substrates (CII inset), CII substrates + ADP (CII+ADP inset), and CIV substrates (CIV inset) in a Na^+-free buffer. p values in this figure represent t test analysis.

(C) Oxygen consumption rates measured in whole CI and P-module mitochondria in Na^+-free buffer (n = 3).

(D) Calibrated TMRM signal in whole CI and P-module mitochondria respiring on CI substrates (CI inset), CII substrates (CII inset), CII substrates + ADP (CII+ADP inset), and CIV substrates (CIV inset) in a Na^+-free buffer (n = 3). p values in this figure represent t test analysis.

(E) Calibrated BCECF-AM signals of whole CI and P-module isolated mitochondria under CI (inset CI-CIII-CIV) and CII substrates (inset CII-CIII-CIV) in a Na^+-free buffer (n = 3). p values in this figure represent t test analysis.

(F and G) Na^+ gradient in WT, CI^{KD}, CI^{KO}, whole CI, and P-module isolated mitochondria incubated with SBFI-AM and respiring on GM (F) or succinate (G), calculated as the ratio of the matrix Na^+ concentrations determined after and before the addition of rotenone (F) or antimycin A (G) (n = 15; n = 13 in CI^{KO}). p values in this figure represent ordinary one-way ANOVA and t test analyses.

(legend continued on next page)

osmotically compensated, Na^+-free buffer. The absence of Na^+ decreased respiration and promoted mitochondrial depolarization by a third or a half, depending on the substrate conditions (Figures 4D, 4E, and S6A). Mouse heart mitochondria behaved similarly (Figures 4F, 4G, and S6B). In parallel, removing Na^+ from the buffer promoted apparently higher CI- and CII-dependent H^+ pumping in WT mitochondria, which is the consequence of an inoperative mNHE, unable to transform the H^+ gradient into a Na^+ gradient (Figures 4H and 4I). None of these phenomena were observed in CI^{KO} mitochondria (Figures 4J–4M), pointing to a role of the Na^+ gradient in the formation of $\Delta\Psi$mt.

If the reason behind the equal respiration and $\Delta\Psi$mt between CI^{KO} and WT in previous experiments (Table S1) was the presence of mNHE in only WT, it is possible that isosmotically removing Na^+ from the buffer could impede its mNHE function. This would make the $\Delta\Psi$mt to rely exclusively on a H^+ gradient in both WT and CI^{KO} and not only in CI^{KO}. Thus, we compared WT and CI^{KO} mitochondrial respiration and $\Delta\Psi$mt in an osmotically compensated, Na^+ free buffer. In contrast with the previous observation, in which we showed equal respiration and $\Delta\Psi$mt between CI^{KO} and WT (Table S1), in the absence of Na^+, we observed higher CII-dependent respiration and hyperpolarization in CI^{KO} in comparison to WT (Figures 5A, 5B, and S6C). Therefore, in the absence of Na^+, the higher CII+III activity in CI^{KO} vs. WT (Table S1) becomes apparent in terms of respiration and $\Delta\Psi$mt. This highlights that an operative mNHE (i.e., WT in the presence of Na^+) is able to dissipate the H^+ gradient, increasing respiration and building up a Na^+ gradient, which contributes to $\Delta\Psi$mt, reaching similar respiratory/$\Delta\Psi$mt values to CI^{KO} despite having lower CII+III activity.

We followed the same reasoning with the P-module mitochondria model. Since these cells display larger mNHE activity (Table S1), the contribution of the Na^+ gradient to $\Delta\Psi$mt should also be larger. Thus, in a Na^+-containing buffer, the P-module mitochondria display higher respiration and $\Delta\Psi$mt than their isogenic counterpart (Table S1). On the contrary, in the absence of Na^+, respiration and $\Delta\Psi$mt would not surpass WT values. As predicted, P-module mitochondria, oxidizing CII or CIV substrates, were not able to raise respiration nor hyperpolarize mitochondria with respect to its isogenic control in the absence of Na^+ (Figures 5C, 5D, and S6D), despite having a slightly larger H^+ pumping even in the absence of Na^+ (Figure 5E). This indicates that, in the presence of an operative mNHE, Na^+ is necessary for the generation of $\Delta\Psi$mt. Thus, having a larger mNHE activity (i.e., in the P-module model) allows a greater contribution of the Na^+ gradient to the generation of $\Delta\Psi$mt, a larger dissipation of the H^+ gradient, and increased respiration.

In a third approach, we directly measured the mitochondrial Na^+ gradient in isolated mitochondria. For respiration driven by CI or CII substrates, the Na^+ gradient in CI^{KD} and CI^{KO} mitochondria was below WT (Figures 5F and 5G). By contrast, the Na^+ gradient in P-module mitochondria was unaffected (Figures 5F and 5G), indicating that the formation of a Na^+ gradient requires a fully assembled CI P-module and mNHE function.

Fourth, if CI was able to build up a Na^+ gradient and contribute to $\Delta\Psi$mt due to its Na^+-selective NHE function in intact mitochondria, NADH-oxidizing CI alone should be able to reproduce such a behavior. To investigate this, pure CI from pig heart mitochondria was reconstituted into liposomes and fed with NADH and decyl-CoQ to activate its H^+ pumping function in the absence or presence of Na^+ (Figure 5H). Active CI was able to create a membrane potential in proteoliposomes through the increase in their H^+ content in the absence of Na^+ (pink lines of left inset and light green of the right inset in Figure 5I). In the presence of Na^+, CI generates an even higher membrane potential at the expense of the H^+ gradient produced by its H^+ pumping function (red lines of left inset and dark green of the right inset in Figure 5I). These results corroborate that active CI contributes to the generation of membrane potential not only through its H^+ pumping function but also through its NHE activity. In intact mitochondria, this H^+-dissipating effect of the CI-dependent mNHE also increases respiration and contributes to the generation of $\Delta\Psi$mt. Since this capacity was absent in CI^{KD} and CI^{KO} models respiring under CII or CIV substrates, these models did not fulfill our expectations based on isolated CII+III/CIV activities. To corroborate that the absence of the H^+ dissipating effect of mNHE constitutes a brake for respiration, we measured respiration under different substrates in permeabilized mitochondria from CI^{KD} and CI^{KO}. In these conditions, a higher CII- and CIV-dependent respiration could be readily seen (Figures 5J, 5K, S6E, and S6F). Altogether, our results show that the mNHE function by CI forms a Na^+ gradient at the expense of H^+ gradient dissipation, which raises respiration and contributes to the buildup of $\Delta\Psi$mt in respiring mitochondria.

The measurements taken throughout this study allow us to calculate that for respiration driven by CI or CII substrates, the Na^+ gradient contributes around one-third of the total $\Delta\Psi$mt (Table S2). However, when CV is activated by the presence of ADP (state 3) and partially dissipates ΔpH, the electrical contribution of the Na^+ gradient reaches approximately half of the $\Delta\Psi$mt (Table S2). The contribution of the Na^+ gradient to $\Delta\Psi$mt in coupled-respiring mitochondria, together with its effects in respiration, were also observed in intact cells (Figures 6A–6E).

A point mutation causing LHON specifically damages CI mNHE function

The fact that the two functions of CI, NADH:CoQ oxidoreductase and mNHE, are independent raised the possibility that mutations

(H) Scheme showing the experimental setup followed in section (J).

(I) Membrane potential (left inset; $n = 4$) or extravesicular pH (right inset; $n = 5$) of proteoliposomes reconstituted with pure CI were measured in a physiological buffer containing 130 μM decyl-CoQ in the presence or absence of 100 mM NaCl and before and after the addition of 100 μM NADH. Each experiment is represented by dotted lines and the mean by a continuous line.

(J) Oxygen consumption rates in WT and CI^{KD} frozen-thawed-permeabilized mitochondria in the presence of cyt c ($n = 3$).

(K) Oxygen consumption rates in WT and CI^{KO} frozen-thawed-permeabilized mitochondria in the presence of cyt c ($n = 3$). Violin plots in this figure show dots representing every replicate and a dotted line indicating the mean of all experiments. Labels are the same as in Figure 2.

See also Figure S6.

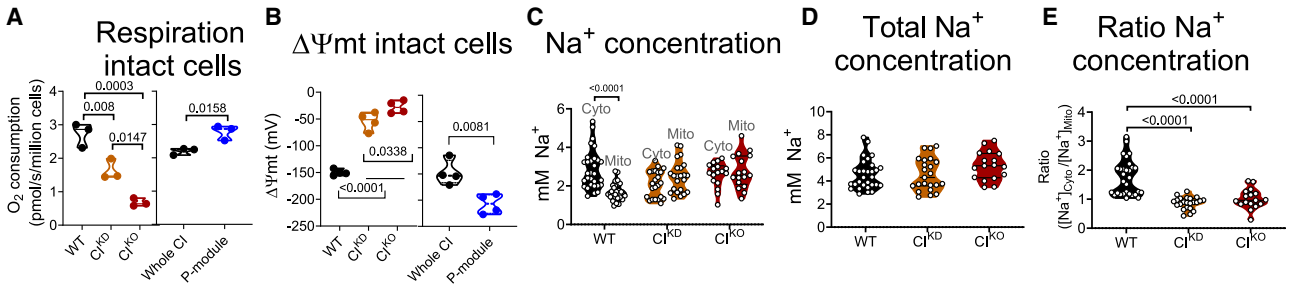

Figure 6. The mitochondrial Na^+ gradient contributes to respiratory rates and ΔΨmt in intact cells

(A) Oxygen consumption in intact WT, CI^{KD}, CI^{KO}, Whole CI, and P-module cells measured by respirometry. *p* values represent ordinary one-way ANOVA and t test analyses.

(B) Calibrated TMRM signal in intact WT, CI^{KD}, CI^{KO}, Whole CI, and P-module cells measured by confocal microscopy. *p* values represent ordinary one-way ANOVA and t test analyses.

(C) Cytosolic and mitochondrial Na^+ concentrations in WT, CI^{KD}, and CI^{KO} intact cells measured by confocal microscopy. *p* values represent a t test analysis.

(D) Total Na^+ concentrations calculated as the sum of cytosolic and mitochondrial Na^+ concentrations, measured by confocal microscopy.

(E) Mitochondrial Na^+ gradient calculated as the ratio between cytosolic and mitochondrial Na^+ concentrations measured by confocal microscopy. *p* values represent an ordinary one-way ANOVA analysis.

Violin plots in this figure show dots representing every replicate and a dotted line indicating the mean of all experiments.

See Table S2.

in key CI P-module residues could only alter mNHE activity. This, subsequently, could alter ΔΨmt independently of the CI NADH:CoQ oxidoreductase and H^+ pumping functions. LHON is a mitochondrial disorder causing central vision loss at early age by degeneration of the optic nerve, and it is produced by mutations in mtDNA-encoded CI subunits. Particularly, 11778G>A mtDNA point mutation in ND4 (Video S1), the most common mutation producing LHON, does not show a detectable decrease in neither CI activity[28,29] (Figures 7A and 7B), CI-III-IV-dependent H^+ pumping in isolated mitochondria (Figure 7C), H^+ pumping in purified CI reconstituted into proteoliposomes (Figure 7D), nor CI assembly (Figure S7A). However, LHON mitochondria displayed higher CII+III activity (Figure 7E) and comparable CIV activity than its control (Figure S7B). Accordingly, LHON mitochondria showed larger CII-III-IV-dependent H^+ pumping (Figure 7F). Very interestingly, LHON mitochondria showed lower mNHE activity compared with its control (Figures 7G and S7C–S7E), and, accordingly, pure CI isolated from LHON cells and reconstituted into proteoliposomes also displayed truncated NHE function in comparison to its isogenic counterpart (Figure 7H). Thus, the CI mutation producing LHON did not cause any defect either in CI assembly, CI-dependent NADH:CoQ oxidoreductase activity, or H^+ pumping, but specifically in the CI-dependent mNHE function. This translated into a lower Na^+ gradient (Figures 7I and 7J), mitochondrial depolarization (Figure 7K), lower membrane potential buildup in pure CI-reconstituted proteoliposomes (Figure 7L), and decreased mitochondrial oxygen consumption under CI substrates (Figure 7M). These results were also reproduced in intact cells (Figures S7F and S7G).

An important factor for the pathogenesis of LHON is the deregulation of mitochondrial Ca^{2+} management, which plays a particularly important role in the opening of the mitochondrial permeability transition pore (mPTP).[30] Given that mitochondrial Ca^{2+} homeostasis is tightly linked to mitochondrial Na^+ homeostasis through the roles of mNHE and NCLX, we wondered whether the reported alterations in Ca^{2+} management in 11778G>A cells could be due to its defect in mNHE. In WT cells, mitochondrial Ca^{2+} entry through MCU activates NCLX, enabling Ca^{2+} exit in an exchange for $3Na^+$. Then, these Na^+ ions are extruded, and H^+ ions are taken into the mitochondria by the action of mNHE. Thus, as mitochondrial Ca^{2+} enters in the matrix, this compartment becomes acidified by mNHE. In this way, given that mNHE function is impaired in LHON, mitochondrial Ca^{2+} entry is expected to induce a slighter pH decrease in its matrix compared with its isogenic control. We first observed that basal mitochondrial Ca^{2+} levels were higher in LHON (Figure S7H) and that mitochondrial Ca^{2+} entry and exit were diminished (Figures 7N and S7I–S7K). These features were not due to alterations in the levels or isolated activities of other proteins involved in the homeostasis of mitochondrial Ca^{2+} (Figures S7K–S7P) or lower cytosolic Ca^{2+} entry (Figure S7Q), indicating that (1) the decrease in mitochondrial Ca^{2+} uptake seen in whole LHON cells was directly caused by the mitochondrial depolarization and (2) that the lower mitochondrial Ca^{2+} exit was exclusively due to lower NHE activity and not due to alterations in NCLX or transmembrane BAX inhibitor motif containing protein 5 (TMBIM5) activities. We then measured mitochondrial matrix pH and observed that, basally, LHON matrix was more acidic (Figure S7R), presumably due to higher CV content and activity (Figures S7A and S7S). Upon mitochondrial Ca^{2+} entry stimulation, WT cells acidified the mitochondrial matrix as would be expected by the action of mNHE. However, the decrease in pH during mitochondrial Ca^{2+} entry in LHON was smaller (Figure S7R). In fact, a similar or even deeper phenotype could be observed in CI^{KO} (Figures S7T and S7U). All these results show that the specific decrease in mNHE activity in LHON not only directly affects ΔΨmt and respiration by depolarizing mitochondria and lowering oxygen consumption, but also alters mitochondrial Ca^{2+} management, causally explaining the molecular pathogenesis of a disease-causing mutation with a previously unknown etiology. Indeed, artificial restoration of Na^+/H^+ antiport with monensin was sufficient to reverse the bioenergetic phenotype in LHON mitochondria (Figure S7V).

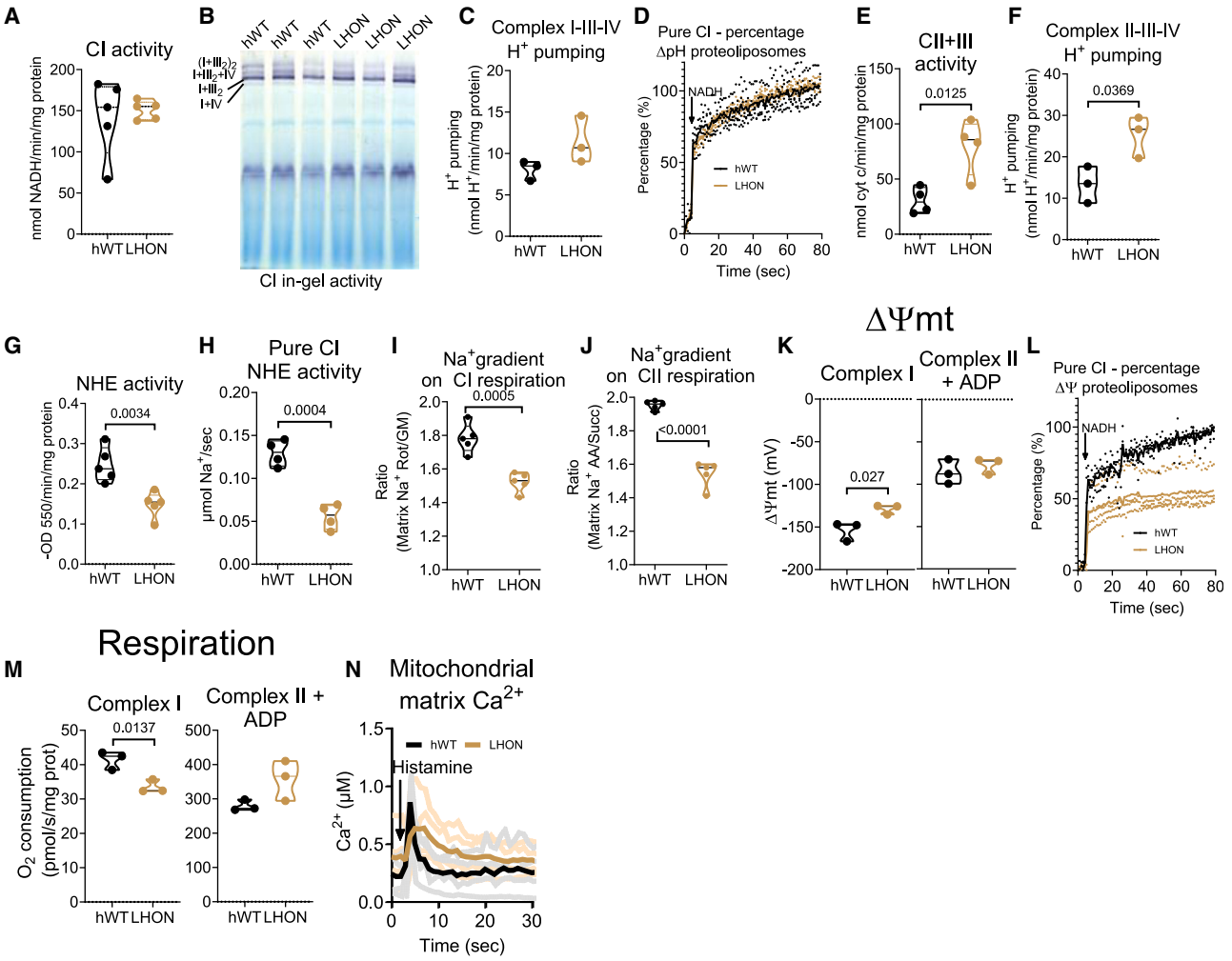

Figure 7. mNHE activity is specifically altered in LHON

(A) Rotenone-sensitive NADH-decylCoQ oxidoreductase activity in LHON vs. control mitochondrial membranes (n = 5).

(B) CI in-gel activity in control (hWT) and LHON mitochondrial samples.

(C) Mitochondrial matrix H^+ pumping measured from the BCEFC-AM signal in hWT and LHON isolated mitochondria respiring on CI substrates in Na^+-containing buffer (n = 3).

(D) Extravesicular pH (n = 4) of proteoliposomes reconstituted with pure CI from hWT and LHON mitochondria measured as in Figure 5I. Each experiment is represented by dotted lines and the mean by a continuous line.

(E) Antimycin A-sensitive succinate-cyt c oxidoreductase activity in LHON vs. hWT mitochondrial membranes (n = 4).

(F) Mitochondrial matrix H^+ pumping measured from the BCEFC-AM signal in hWT and LHON isolated mitochondria respiring on CII substrates in Na^+-containing buffer (n = 3).

(G) Passive swelling reverse NHE activity measured in hWT vs. LHON mitochondria (n = 5).

(H) Buffer Na^+ content was measured as in Figure 1B to test forward NHE (n = 4).

(I and J) Na^+ gradient in hWT vs. LHON isolated mitochondria, incubated with SBFI-AM and respiring on GM (I) or succinate (J), and calculated as the ratio of the matrix Na^+ concentrations determined before and after the addition of rotenone (I) or antimycin A (J; n = 5).

(K) Calibrated TMRM signal measured in hWT vs. LHON respiring with CI or CII+ADP substrates (n = 3).

(L) Membrane potential (n = 4) of proteoliposomes reconstituted with pure CI from hWT and LHON mitochondria measured as in Figure 5I. Each experiment is represented by dotted lines and the mean by a continuous line.

(M) Oxygen consumption measured in hWT vs. LHON respiring with CI or CII+ADP substrates (n = 3).

(N) Mitochondrial Ca^{2+} measured with calibrated Cepia2mt in hWT vs. LHON cells before and after stimulation with 100 µM histamine (n = 4). Each experiment is represented by semi-transparent lines and the mean by an opaque line.

Violin plots in this figure show dots representing every replicate and a dotted line indicating the mean of all experiments. p values represent t test analyses. See Figure S7.

DISCUSSION

In this work, we provide strong evidence supporting that CI conducts the mNHE activity in mammalian mitochondria. By using pure CI, a rainbow of genetic models, and a biochemical characterization, we showed that, specifically, the P-module of CI performs the mNHE activity. This may explain why the yeast *Saccharomyces cerevisiae* (*S. cerevisiae*) (i.e., organism lacking CI) does not possess mNHE function.[31] Next, we employed mNHE loss-of-function and gain-of-function models to study the role of mNHE function in bioenergetics. mNHE dissipates the H^+ gradient, increasing respiration and creating, in turn, a Na^+ gradient across the IMM. This Na^+ gradient contributes up to half of the $\Delta\Psi$mt in coupled-respiring mitochondria. We have also studied the 11778G>A mtDNA point mutation in ND4 that causes LHON and observed that this model had a decreased mNHE activity while maintaining intact CI assembly, super-assembly, and its other CI-dependent activities. Deregulation of mNHE in this model also produced lower respiration and mitochondrial depolarization, as well as a severe defect in mitochondrial Ca^{2+} management, causally explaining the molecular pathogenesis of this disease.

The presence of mNHE function, as well as the associated formation of a mitochondrial Na^+ gradient, enables the control of $\Delta\Psi$mt, in addition to ΔpH, and a more efficient use of substrates in terms of oxygen consumption. First, the fact that mNHE dissipates the H^+ gradient to build a Na^+ gradient highlights the fact that ΔpH and $\Delta\Psi$mt are exchangeable parameters in Peter Mitchell's equation of Δp. Consequently, the Na^+ gradient acts as a reservoir for $\Delta\Psi$mt. Also, there may be (patho)physiological situations in which $\Delta\Psi$mt is maintained high at the expense of a low ΔpH; this would make $\Delta\Psi$mt less dependent of CV activity and ATP generation, for instance. Second, substrate oxidation and oxygen consumption are facilitated by mNHE. Given that accumulation of H^+ in the IMS halts respiration, the H^+-dissipating effect of mNHE permits an increase in substrate oxidation and a concomitant raise in respiration. This, in turn, results in the formation of a Na^+ gradient, which contributes to the buildup of $\Delta\Psi$mt.

It is also possible that a higher mNHE activity increases respiration in models with impaired substrate oxidation, reaching WT values. Such as the case of the P-module mitochondria respiring under CI substrates. Despite having lower CI activity (Figure S2D), they showed similar respiration and $\Delta\Psi$mt values under CI substrates compared with their isogenic control when they were functioning in a buffer with Na^+ (Figures 2G and 2H). This apparently contradictory finding was easily explained by the fact that P-module mitochondria had higher mNHE activity and that the contribution of the Na^+ gradient to the $\Delta\Psi$mt was larger in this model. Indeed, removing Na^+ from the respiratory buffer was enough to observe a decreased respiration and depolarization in P-module mitochondria under CI substrates (Figures 5C and 5E). This highlights that P-module mitochondria built up a Na^+ gradient-dependent $\Delta\Psi$mt sufficient to mask its lower CI NADH:CoQ oxidoreductase activity and that this effect was due to its higher mNHE activity. Such an intricate effect calls for caution when assessing O_2 consumption and $\Delta\Psi$mt since, in general, the presence/absence of Na^+ yield divergent results and, in particular, different CI-deficiency models display different mNHE activities.

The discovery that a transmitochondrial Na^+ gradient controls $\Delta\Psi$mt, together with its tight regulation by a non-canonical mNHE function of CI, introduces an unexpected layer of regulation to mitochondrial bioenergetics, metabolism, and ion management in mammalian mitochondria. This activity may contribute to the versatility of mitochondrial roles found in complex organisms, in which different cell types utilize mitochondria for divergent purposes. In particular, and as shown in the present work, the generation of a transmitochondrial Na^+ gradient is a critical feature for mitochondrial biology, with extensive impact for neuronal physiology and disease.

Limitations of the study

Our study demonstrates the existence of a transmitochondrial Na^+ gradient in mammalian mitochondria, which controls $\Delta\Psi$mt, generated by the activity of the fast-acting, Na^+-specific mNHE, which we identified as CI. However, it should be noted that intramitochondrial differences in the Na^+ gradient could not be established as the resolution of probes and techniques does not allow this level of analysis.

Another limitation lies in the fact that, though in this work we have discovered that the mitochondrial Na^+ gradient (1) parallels the H^+ gradient and (2) that such a gradient contributes up to half of the $\Delta\Psi$mt in coupled mammalian mitochondria, it does not provide an explanation on how such small Na^+ or H^+ gradients (of about 2out:1in) are able to generate such large potentials ($-$180 mV) across the IMM. Future work is guaranteed to solve this apparent discrepancy.

A strong difficulty of this work is that we have done an effort to provide quantitative bioenergetics through all the study. This set of measurements is particularly difficult given the varying nature of this parameter, depending on the culture conditions (confluency, time to stabilize under a specific temperature, time after extraction of mitochondria, substrates in the culture medium, etc.) and experimental settings (buffer osmolarity, density, viscosity, ionic strength, ion permeability, time to stabilize under a specific temperature, time of prepared stock reagents, etc.). Thus, extreme carefulness must be taken when performing these experiments. However, despite these difficulties, we believe that quantitative measurements are of paramount importance to the bioenergetics field since, for instance, many cellular pathways depend on $\Delta\Psi$mt, which are triggered by reaching a particular threshold of mitochondrial depolarization. Also, quantitative analysis of this parameter could inform about substrate availability in whole cells or reactive oxygen species (ROS) production in any type of experimental platform.[32]

In the bioenergetic field, it has been proposed that a K^+ gradient controlled $\Delta\Psi$mt in mammalian mitochondria, a hypothesis sustained on the large K^+ abundance in cellular compartments and considered necessary due to the fact that H^+ are buffered at both sides of the mitochondrial inner membrane.[33] However, it should be noted that the K^+ gradient in mitochondria is nearly zero,[33] and its permeability, as reflected in Figure S2K, is extremely low. Thus, its contribution to the total $\Delta\Psi$mt, calculated by the Nernst equation, is expected to be minimal. In addition, K^+ is a well-known controller of mitochondrial volume, a variable affecting the generation of $\Delta\Psi$mt. However, we have not studied the specific contribution of K^+ to the $\Delta\Psi$mt, and, thus, our

considerations in this regard are only theoretical. Thus, further efforts should be provided to determine the exact role of K^+ in the generation of $\Delta\Psi$mt. On the other hand, the unbuffered Na^+ gradient exists together with an exceptionally high mitochondrial Na^+ permeability provided by the mNHE. Therefore, its contribution to the $\Delta\Psi$mt, calculated by the Nernst equation, is expected to be relevant, as experimentally demonstrated in this manuscript.

RESOURCE AVAILABILITY

Lead contact

Further information and requests for resources and reagents should be directed to and will be fulfilled by the lead contact, José Antonio Enríquez (jaenriquez@cnic.es).

Materials availability

Cell lines used and generated in this study are available from the lead contact upon a Materials Transfer Agreement. This study did not generate new, unique reagents or mouse lines.

Data and code availability

- Raw data have been deposited at Mendeley and are publicly available as of the date of publication. Accession numbers are listed in the key resources table.
- This paper does not report original code.
- Any additional information required to reanalyze the data reported in this work paper is available from the lead contact upon request.

ACKNOWLEDGMENTS

We thank Dr. Cogliati (CMBSO, UAM-CSIC) for helping with TEM imaging; Dr. Curtabbi, Drs. Castillo & Priori (CNIC), and Dr. Rial (CIB-CSIC) for fruitful discussion; and MM Muñoz-Hernandez, R Martínez-de-Mena, E.R. Martínez-Jiménez, and C. Jiménez for technical assistance. We acknowledge Dr. Moreno-Loshuertos and Dr. Sancho for kindly providing cell line models. Scheme figures were made with BioRender. We thank Dr. Calvo-Adiego from Incarlopsa Slaughterhouse for the generous gift of fresh porcine heart. Microscopy was performed in the Microscopy and Dynamic Imaging Unit.

Funding is as follows: this study was supported by competitive grants from the Ministerio de Ciencia e Innovación (MCIN) RTI2018-099357-B-I00, CIBERFES (CB16/10/00282), Human Frontier Science Program (grant RGP0016/2018), and Leducq Transatlantic Networks (17CVD04) to J.A.E. P.H.-A. is supported by a JdC IJC2020-042679-I, and Y.M.-M. is supported by an FPI-SO fellowship PRE2018-083478. The CNIC is supported by the Instituto de Salud Carlos III (ISCIII), the Ministerio de Ciencia, Innovación y Universidades (MICIU), and the Pro CNIC Foundation, and is a Severo Ochoa Center of Excellence (grant CEX2020-001041-S funded by MICIU/AEI/10.13039/501100011033). I.L.-M. acknowledges financial support through the TECNOLOGÍAS 2018 program funded by the Regional Government of Madrid (grant S2018/BAA-4403 SINOXPHOS-CM).

AUTHOR CONTRIBUTIONS

Conceptualization, P.H.-A. and J.A.E.; methodology, P.H.A., C.M.-V., R.A.-P. (BN-PAGE of pure CI and OXPHOS mutants), Y.M.-M. (Opa1 western blot), P.N., I.L.-M. (purification and reconstitution of CI in proteoliposomes), E.C. (proteomics), S.N.J. (microcopy), and J.L.C.-A. (bioinformatics); investigation, P.H.-A.; funding acquisition, J.A.E. and J.V.; project administration, J.A.E.; writing, P.H.-A. and J.A.E.; writing – review & editing, P.H.-A., Y.M.-M., S.N.J., P.N., I.L.-M., E.C., J.V., and J.A.E.

DECLARATION OF INTERESTS

The authors declare no competing interests.

STAR★METHODS

Detailed methods are provided in the online version of this paper and include the following:

- KEY RESOURCES TABLE
- EXPERIMENTAL MODEL AND STUDY PARTICIPANT DETAILS
  - Animal models
  - Cell culture and treatment
- METHOD DETAILS
  - Mitochondria isolation
  - Mitochondrial membrane isolation and measurement of complex activities
  - Measurement of O_2 consumption and mitochondrial membrane potential
  - Blue native gel electrophoresis
  - SDS gel electrophoresis
  - Immunodetection of single proteins, complexes, and supercomplexes
  - Measurement of mitochondrial ATP synthesis
  - Measurements of mitochondrial matrix Na^+ and H^+
  - Spectrophotometric swelling assay in isolated mitochondria
  - Measurement of Na^+ gradient in whole cells by confocal microscopy
  - Measurement of mitochondrial Ca^{2+} and pH, and cytosolic Ca^{2+} in whole cells by confocal microscopy
  - Measurement of $\Delta\Psi$mt in whole cells by confocal microscopy
  - Measurement of mitochondrial volume
  - Transmission electron microscopy
  - LHON mutation structural modelling
  - Proteomic analysis
  - Purification of Porcine Heart Complex I
  - Reconstitution of Complex I into proteoliposomes
  - Measurement of Pure Complex I NHE activity and membrane potential into proteoliposomes
  - Analysis of mitochondrial morphology by confocal microscopy
  - Measurement of H^+ movement by electrophysiology
  - Measurement of isolated and NHE-linked mitochondrial channel activities
- QUANTIFICATION AND STATISTICAL ANALYSIS

SUPPLEMENTAL INFORMATION

Supplemental information can be found online at https://doi.org/10.1016/j.cell.2024.08.045.

Received: January 22, 2024
Revised: July 2, 2024
Accepted: August 21, 2024
Published: September 19, 2024

REFERENCES

1. Hernansanz-Agustín, P., and Enríquez, J.A. (2021). Functional segmentation of CoQ and cyt c pools by respiratory complex superassembly. Free Radic. Biol. Med. *167*, 232–242. https://doi.org/10.1016/j.freeradbiomed.2021.03.010.
2. Mitchell, P. (1961). Coupling of phosphorylation to electron and hydrogen transfer by a chemi-osmotic type of mechanism. Nature *191*, 144–148. https://doi.org/10.1038/191144a0.
3. Nicholls, D.G. (1974). The influence of respiration and ATP hydrolysis on the proton-electrochemical gradient across the inner membrane of rat-liver mitochondria as determined by ion distribution. Eur. J. Biochem. *50*, 305–315. https://doi.org/10.1111/j.1432-1033.1974.tb03899.x.
4. Agip, A.A., Blaza, J.N., Fedor, J.G., and Hirst, J. (2019). Mammalian Respiratory Complex I Through the Lens of Cryo-EM. Annu. Rev. Biophys. *48*, 165–184. https://doi.org/10.1146/annurev-biophys-052118-115704.

5. Kampjut, D., and Sazanov, L.A. (2022). Structure of respiratory complex I - An emerging blueprint for the mechanism. Curr. Opin. Struct. Biol. *74*, 102350. https://doi.org/10.1016/j.sbi.2022.102350.

6. Parey, K., Brandt, U., Xie, H., Mills, D.J., Siegmund, K., Vonck, J., Kühlbrandt, W., and Zickermann, V. (2018). Cryo-EM structure of respiratory complex I at work. eLife *7*, e39213. https://doi.org/10.7554/eLife.39213.

7. Hamamoto, T., Hashimoto, M., Hino, M., Kitada, M., Seto, Y., Kudo, T., and Horikoshi, K. (1994). Characterization of a gene responsible for the Na+/H+ antiporter system of alkalophilic Bacillus species strain C-125. Mol. Microbiol. *14*, 939–946. https://doi.org/10.1111/j.1365-2958.1994.tb01329.x.

8. Poburko, D., and Demaurex, N. (2012). Regulation of the mitochondrial proton gradient by cytosolic Ca(2)(+) signals. Pflugers Arch. *464*, 19–26. https://doi.org/10.1007/s00424-012-1106-y.

9. Palty, R., Silverman, W.F., Hershfinkel, M., Caporale, T., Sensi, S.L., Parnis, J., Nolte, C., Fishman, D., Shoshan-Barmatz, V., Herrmann, S., et al. (2010). NCLX is an essential component of mitochondrial Na+/Ca2+ exchange. Proc. Natl. Acad. Sci. USA *107*, 436–441. https://doi.org/10.1073/pnas.0908099107.

10. Hernansanz-Agustín, P., and Enríquez, J.A. (2022). Sodium in Mitochondrial Redox Signaling. Antioxid. Redox Signal. *37*, 290–300. https://doi.org/10.1089/ars.2021.0262.

11. Blondin, G.A., Vail, W.J., and Green, D.E. (1969). The mechanism of mitochondrial swelling. II. Pseudoenergized swelling in the presence of alkali metal salts. Arch. Biochem. Biophys. *129*, 158–172. https://doi.org/10.1016/0003-9861(69)90162-3.

12. Brierley, G.P., Davis, M.H., Cragoe, E.J., Jr., and Jung, D.W. (1989). Kinetic properties of the Na+/H+ antiport of heart mitochondria. Biochemistry *28*, 4347–4354. https://doi.org/10.1021/bi00436a034.

13. Brierley, G.P., Davis, M.H., and Jung, D.W. (1988). Intravesicular pH changes in submitochondrial particles induced by monovalent cations: relationship to the Na+/H+ and K+/H+ antiporters. Arch. Biochem. Biophys. *264*, 417–427. https://doi.org/10.1016/0003-9861(88)90307-4.

14. Brierley, G.P., Jurkowitz, M., and Jung, D.W. (1978). Osmotic swelling of heart mitochondria in acetate and chloride salts. Evidence for two pathways for cation uptake. Arch. Biochem. Biophys. *190*, 181–192. https://doi.org/10.1016/0003-9861(78)90266-7.

15. Douglas, M.G., and Cockrell, R.S. (1974). Mitochondrial cation-hydrogen ion exchange. Sodium selective transport by mitochondria and submitochondrial particles. J. Biol. Chem. *249*, 5464–5471. https://doi.org/10.1016/S0021-9258(20)79751-6.

16. Mitchell, P., and Moyle, J. (1967). Respiration-driven proton translocation in rat liver mitochondria. Biochem. J. *105*, 1147–1162. https://doi.org/10.1042/bj1051147.

17. Nakashima, R.A., and Garlid, K.D. (1982). Quinine inhibition of Na+ and K+ transport provides evidence for two cation/H+ exchangers in rat liver mitochondria. J. Biol. Chem. *257*, 9252–9254. https://doi.org/10.1016/S0021-9258(18)34058-4.

18. Stolpe, S., and Friedrich, T. (2004). The Escherichia coli NADH:ubiquinone oxidoreductase (complex I) is a primary proton pump but may be capable of secondary sodium antiport. J. Biol. Chem. *279*, 18377–18383. https://doi.org/10.1074/jbc.M311242200.

19. Batista, A.P., Marreiros, B.C., and Pereira, M.M. (2011). Decoupling of the catalytic and transport activities of complex I from Rhodothermus marinus by sodium/proton antiporter inhibitor. ACS Chem. Biol. *6*, 477–483. https://doi.org/10.1021/cb100380y.

20. Roberts, P.G., and Hirst, J. (2012). The deactive form of respiratory complex I from mammalian mitochondria is a Na+/H+ antiporter. J. Biol. Chem. *287*, 34743–34751. https://doi.org/10.1074/jbc.M112.384560.

21. Carelli, V., Ghelli, A., Bucchi, L., Montagna, P., De Negri, A., Leuzzi, V., Carducci, C., Lenaz, G., Lugaresi, E., and Degli Esposti, M. (1999). Biochemical features of mtDNA 14484 (ND6/M64V) point mutation associated with Leber's hereditary optic neuropathy. Ann. Neurol. *45*, 320–328. https://doi.org/10.1002/1531-8249(199903)45:3<320::AID-ANA7>3.0.CO;2-L.

22. Kampjut, D., and Sazanov, L.A. (2020). The coupling mechanism of mammalian respiratory complex I. Science *370*. https://doi.org/10.1126/science.abc4209.

23. Acín-Pérez, R., Carrascoso, I., Baixauli, F., Roche-Molina, M., Latorre-Pellicer, A., Fernández-Silva, P., Mittelbrunn, M., Sanchez-Madrid, F., Pérez-Martos, A., Lowell, C.A., et al. (2014). ROS-triggered phosphorylation of complex II by Fgr kinase regulates cellular adaptation to fuel use. Cell Metab. *19*, 1020–1033. https://doi.org/10.1016/j.cmet.2014.04.015.

24. Perales-Clemente, E., Fernández-Vizarra, E., Acín-Pérez, R., Movilla, N., Bayona-Bafaluy, M.P., Moreno-Loshuertos, R., Pérez-Martos, A., Fernández-Silva, P., and Enríquez, J.A. (2010). Five entry points of the mitochondrially encoded subunits in mammalian complex I assembly. Mol. Cell. Biol. *30*, 3038–3047. https://doi.org/10.1128/MCB.00025-10.

25. Guarás, A., Perales-Clemente, E., Calvo, E., Acín-Pérez, R., Loureiro-Lopez, M., Pujol, C., Martínez-Carrascoso, I., Nuñez, E., García-Marqués, F., Rodríguez-Hernández, M.A., et al. (2016). The CoQH2/CoQ Ratio Serves as a Sensor of Respiratory Chain Efficiency. Cell Rep. *15*, 197–209. https://doi.org/10.1016/j.celrep.2016.03.009.

26. Bianchi, C., Genova, M.L., Parenti Castelli, G., and Lenaz, G. (2004). The mitochondrial respiratory chain is partially organized in a supercomplex assembly: kinetic evidence using flux control analysis. J. Biol. Chem. *279*, 36562–36569. https://doi.org/10.1074/jbc.M405135200.

27. Mitchell, P. (1978). David Keilin's Respiratory Chain Concept and its Chemiosmotic Consequences. https://www.nobelprize.org/prizes/chemistry/1978/mitchell/lecture/.

28. Hofhaus, G., Johns, D.R., Hurko, O., Attardi, G., and Chomyn, A. (1996). Respiration and growth defects in transmitochondrial cell lines carrying the 11778 mutation associated with Leber's hereditary optic neuropathy. J. Biol. Chem. *271*, 13155–13161. https://doi.org/10.1074/jbc.271.22.13155.

29. Larsson, N.G., Andersen, O., Holme, E., Oldfors, A., and Wahlström, J. (1991). Leber's hereditary optic neuropathy and complex I deficiency in muscle. Ann. Neurol. *30*, 701–708. https://doi.org/10.1002/ana.410300511.

30. Kirches, E. (2011). LHON: Mitochondrial Mutations and More. Curr. Genomics *12*, 44–54. https://doi.org/10.2174/138920211794520150.

31. Welihinda, A.A., Trumbly, R.J., Garlid, K.D., and Beavis, A.D. (1993). On the regulation of Na+/H+ and K+/H+ antiport in yeast mitochondria: evidence for the absence of an Na(+)-selective Na+/H+ antiporter. Biochim. Biophys. Acta *1144*, 367–373. https://doi.org/10.1016/0005-2728(93)90122-v.

32. Scaduto, R.C., Jr., and Grotyohann, L.W. (1999). Measurement of mitochondrial membrane potential using fluorescent rhodamine derivatives. Biophys. J. *76*, 469–477. https://doi.org/10.1016/S0006-3495(99)77214-0.

33. Garlid, K.D., and Paucek, P. (2003). Mitochondrial potassium transport: the K(+) cycle. Biochim. Biophys. Acta *1606*, 23–41. https://doi.org/10.1016/s0005-2728(03)00108-7.

34. Fernández-Vizarra, E., Ferrín, G., Pérez-Martos, A., Fernández-Silva, P., Zeviani, M., and Enríquez, J.A. (2010). Isolation of mitochondria for biogenetical studies: An update. Mitochondrion *10*, 253–262. https://doi.org/10.1016/j.mito.2009.12.148.

35. Morava, E., Rodenburg, R.J., Hol, F., de Vries, M., Janssen, A., van den Heuvel, L., Nijtmans, L., and Smeitink, J. (2006). Clinical and biochemical characteristics in patients with a high mutant load of the mitochondrial T8993G/C mutations. Am. J. Med. Genet. A *140*, 863–868. https://doi.org/10.1002/ajmg.a.31194.

36. Ross, M.F., Prime, T.A., Abakumova, I., James, A.M., Porteous, C.M., Smith, R.A., and Murphy, M.P. (2008). Rapid and extensive uptake and activation of hydrophobic triphenylphosphonium cations within cells. Biochem. J. *411*, 633–645. https://doi.org/10.1042/BJ20080063.

37. Wittig, I., Braun, H.P., and Schägger, H. (2006). Blue native PAGE. Nat. Protoc. *1*, 418–428. https://doi.org/10.1038/nprot.2006.62.

38. Hernansanz-Agustín, P., Choya-Foces, C., Carregal-Romero, S., Ramos, E., Oliva, T., Villa-Piña, T., Moreno, L., Izquierdo-Álvarez, A., Cabrera-García, J.D., Cortés, A., et al. (2020). Na(+) controls hypoxic signalling by the mitochondrial respiratory chain. Nature *586*, 287–291. https://doi.org/10.1038/s41586-020-2551-y.

39. Vives-Bauza, C., Yang, L., and Manfredi, G. (2007). Assay of mitochondrial ATP synthesis in animal cells and tissues. Methods Cell Biol. *80*, 155–171. https://doi.org/10.1016/S0091-679X(06)80007-5.

40. Dlasková, A., Hlavatá, L., Jezek, J., and Jezek, P. (2008). Mitochondrial Complex I superoxide production is attenuated by uncoupling. Int. J. Biochem. Cell Biol. *40*, 2098–2109. https://doi.org/10.1016/j.biocel.2008.02.007.

41. Gerencser, A.A., Chinopoulos, C., Birket, M.J., Jastroch, M., Vitelli, C., Nicholls, D.G., and Brand, M.D. (2012). Quantitative measurement of mitochondrial membrane potential in cultured cells: calcium-induced de- and hyperpolarization of neuronal mitochondria. J. Physiol. *590*, 2845–2871. https://doi.org/10.1113/jphysiol.2012.228387.

42. Laurent, G.J., and Shapiro, S.D. (2006). Encyclopedia of Respiratory Medicine (Academic Press Elsevier).

43. Navarro, P., and Vázquez, J. (2009). A refined method to calculate false discovery rates for peptide identification using decoy databases. J. Proteome Res. *8*, 1792–1796. https://doi.org/10.1021/pr800362h.

44. Bonzon-Kulichenko, E., Garcia-Marques, F., Trevisan-Herraz, M., and Vázquez, J. (2015). Revisiting peptide identification by high-accuracy mass spectrometry: problems associated with the use of narrow mass precursor windows. J. Proteome Res. *14*, 700–710. https://doi.org/10.1021/pr5007284.

45. Trevisan-Herraz, M., Bagwan, N., García-Marqués, F., Rodriguez, J.M., Jorge, I., Ezkurdia, I., Bonzon-Kulichenko, E., and Vázquez, J. (2019). SanXoT: a modular and versatile package for the quantitative analysis of high-throughput proteomics experiments. Bioinformatics *35*, 1594–1596. https://doi.org/10.1093/bioinformatics/bty815.

46. Prieto, G., and Vázquez, J. (2020). Protein Probability Model for High-Throughput Protein Identification by Mass Spectrometry-Based Proteomics. J. Proteome Res. *19*, 1285–1297. https://doi.org/10.1021/acs.jproteome.9b00819.

47. García-Marqués, F., Trevisan-Herraz, M., Martínez-Martínez, S., Camafeita, E., Jorge, I., Lopez, J.A., Méndez-Barbero, N., Méndez-Ferrer, S., Del Pozo, M.A., Ibáñez, B., et al. (2016). A Novel Systems-Biology Algorithm for the Analysis of Coordinated Protein Responses Using Quantitative Proteomics. Mol. Cell. Proteomics *15*, 1740–1760. https://doi.org/10.1074/mcp.M115.055905.

48. Smith, A.L. (1967). [13] Preparation, properties, and conditions for assay of mitochondria: slaughterhouse material, small-scale. Methods Enzymol. *10*, 81–86. https://doi.org/10.1016/0076-6879(67)10016-5.

49. Letts, J.A., Degliesposti, G., Fiedorczuk, K., Skehel, M., and Sazanov, L.A. (2016). Purification of Ovine Respiratory Complex I Results in a Highly Active and Stable Preparation. J. Biol. Chem. *291*, 24657–24675. https://doi.org/10.1074/jbc.M116.735142.

50. Brundage, L., Hendrick, J.P., Schiebel, E., Driessen, A.J., and Wickner, W. (1990). The purified E. coli integral membrane protein SecY/E is sufficient for reconstitution of SecA-dependent precursor protein translocation. Cell *62*, 649–657. https://doi.org/10.1016/0092-8674(90)90111-q.

51. Chaudhry, A., Shi, R., and Luciani, D.S. (2020). A pipeline for multidimensional confocal analysis of mitochondrial morphology, function, and dynamics in pancreatic beta-cells. Am. J. Physiol. Endocrinol. Metab. *318*, E87–E101. https://doi.org/10.1152/ajpendo.00457.2019.

52. Luongo, T.S., Lambert, J.P., Gross, P., Nwokedi, M., Lombardi, A.A., Shanmughapriya, S., Carpenter, A.C., Kolmetzky, D., Gao, E., van Berlo, J.H., et al. (2017). The mitochondrial Na(+)/Ca(2+) exchanger is essential for Ca(2+) homeostasis and viability. Nature *545*, 93–97. https://doi.org/10.1038/nature22082.

53. Carafoli, E., Tiozzo, R., Lugli, G., Crovetti, F., and Kratzing, C. (1974). The release of calcium from heart mitochondria by sodium. J. Mol. Cell. Cardiol. *6*, 361–371. https://doi.org/10.1016/0022-2828(74)90077-7.

STAR★METHODS

KEY RESOURCES TABLE

REAGENT or RESOURCE	SOURCE	IDENTIFIER
Antibodies		
Rabbit Polyclonal NDUFB7 antibody	Proteintech	Cat#ab14912-1-AP
Rabbit Monoclonal NDUFV2 antibody	Abcam	Cat#ab183717
Mouse Monoclonal NDUFA9 antibody	Abcam	Cat#ab14713
Rabbit UQCRC2 Polyclonal Antibody	Proteintech	Cat#14742-1-AP; RRID: AB_2241442
SDHA Mouse Monoclonal Antibody	Invitrogen	Cat#459200; RRID: AB_10838019
MTCO1 Mouse Monoclonal Antibody	Invitrogen	Cat#459600; RRID: AB_10374492
Mouse Monoclonal ATPB antibody	Abcam	Cat#ab14730
Rabbit Polyclonal OPA1 antibody	Abcam	Cat#ab42364
Chemicals, Peptides, and Recombinant Proteins		
Gibco™ DMEM	Fisher scientific	Cat#11965092
Gibco™ Penicillin-Streptomycin (10,000 U/mL)	Fisher scientific	Cat#15-140-122
Rotenone	Sigma-Aldrich	Cat#R8875
Ethylenediaminetetraacetic acid (EDTA)	Sigma-Aldrich	Cat#E9884
NADH	Sigma-Aldrich	Cat#10128023001
Decylubiquinone	Sigma-Aldrich	Cat#D7911
Antimycin A	Sigma-Aldrich	Cat#A8674
Cytochrome c from bovine heart	Sigma-Aldrich	Cat#C2037
Potassium cyanide	Sigma-Aldrich	Cat#207810
Oligomycin A	Sigma-Aldrich	Cat#495455
Pyruvate Kinase (PK)	Sigma-Aldrich	Cat#10109045001
Phosphoenol-pyruvate (PEP)	Sigma-Aldrich	Cat#10108294001
Lactate Dehydrogenase (LDH)	Sigma-Aldrich	Cat#10127230001
ATP	Sigma-Aldrich	Cat#A2383
FCCP	Sigma-Aldrich	Cat#2920
Tetramethylrhodamine, Methyl Ester (TMRM)	ThermoFisher	Cat#T668
Digitonin	Sigma-Aldrich	Cat#D5628
L-Glutamic acid, monosodium salt hydrate	Sigma-Aldrich	Cat#G1626
L-Malic acid	Sigma-Aldrich	Cat#M1000
Sodium succinate dibasic hexahydrate	Sigma-Aldrich	Cat#S2378
ADP	Sigma-Aldrich	Cat#117105
N,*N*,*N*',*N*'-Tetramethyl-*p*-phenylenediamine dihydrochloride, TMPD	Sigma-Aldrich	Cat#T3134
(+)-Sodium L-ascorbate	Sigma-Aldrich	Cat#A7631
Sodium azide	Sigma-Aldrich	Cat#S2002
L-Glutamic acid	Sigma-Aldrich	Cat#G1251
Succinic acid	Sigma-Aldrich	Cat#398055
Phosphoric acid	Sigma-Aldrich	Cat#466123
N-methyl-D-Glucamine (NMDG)	Sigma-Aldrich	Cat#M2004
Protease Inhibitor Cocktail	Sigma-Aldrich	Cat#11836170001
Triton™ X-100	Sigma-Aldrich	Cat#X100
Sodium deoxycholate	Sigma-Aldrich	Cat#D6750
20% SDS Solution	Bio-Rad	Cat#1610418
Glycerol ≥99.0%	Sigma-Aldrich	Cat#G5516
2-Mercaptoethanol	Sigma-Aldrich	Cat#M3148
Bromophenol blue	Sigma-Aldrich	Cat#114391

(*Continued on next page*)

Continued

REAGENT or RESOURCE	SOURCE	IDENTIFIER
Immobilon-FL, 0.45 μm	Merck Millipore	Cat#IPFL00010
TWEEN® 20	Sigma-Aldrich	Cat#P9416
BCECF, AM	Invitrogen	Cat#B1170
SBFI, AM	Invitrogen	Cat#S1263
Nigericin sodium salt	Sigma-Aldrich	Cat#N7143
Monensin sodium salt	Sigma-Aldrich	Cat#M5273
Gramicidin from *Bacillus aneurinolyticus* (*Bacillus brevis*)	Sigma-Aldrich	Cat#G5002
Potassium acetate	Sigma-Aldrich	Cat#P1190
Sodium acetate	Sigma-Aldrich	Cat#Sodium acetate
Ammonium acetate	Sigma-Aldrich	Cat#A7262
Gibco™ HBSS	Fisher Scientific	Cat#14025092
Asante NaTRIUM Green-2 (AM)	Mo Bi Tec Molecular Biotechnology	Cat#3512
CoroNa Red (RedNa Chloride)	BOC Sciences	Cat#A14-0115
Histamine	Sigma-Aldrich	Cat#H7125
Ionomycin, Calcium Salt	Thermo Fisher	Cat#I24222
Potassium hexacyanoferrate(III)	Sigma-Aldrich	Cat#244023
Acridine Orange hydrochloride hydrate	Sigma-Aldrich	Cat#318337
BCECF Acid	Invitrogen	Cat#B1151
SBFI, Tetraammonium Salt	Invitrogen	Cat#10033152
MitoTracker™ Deep Red FM Dye	Invitrogen	Cat#M46753
Luciferase	Merck	Cat#10411523001
Paraformaldehyde Aqueous Solution EM Grade	Electron Microscopy Sciences	Cat#15700
DAPI	Invitrogen	Cat#D1306
ProLong™ Gold Antifade Mountant	Invitrogen	Cat#P36930
Ru360	Merck	Cat#557440
Fluo-4, AM, cell permeant	Invitrogen	Cat#F14201
Sucrose	Sigma-Aldrich	Cat#S0389
Tris/ Trizma® Base	Sigma-Aldrich	Cat#T1503
DL-Dithiothreitol (DTT)	Sigma-Aldrich	Cat#D0632
1-palmitoyl-2-oleoyl-glycero-3-phosphocholine (POPC)	Avanti	Cat#850457P
Cardiolipin (Heart, Bovine) (sodium salt)	Avanti	Cat#840012
n-Dodecyl-β-D-Maltopyranoside (DDM)	Anatrace	Cat#D310
4-(2-Hydroxyethyl)piperazine-1-ethanesulfonic acid, N-(2-Hydroxyethyl)piperazine-N′-(2-ethanesulfonic acid) (HEPES)	Sigma-Aldrich	Cat#H3375
Sucrose BioXtra, ≥99.5% (GC), 250G	Merck Life Science, S.L.U.	Cat#S7903-250G
IODOACETAMIDE BIOULTRA SIGMA-ALDRICH	Mervilab	Cat#I1149-25G
Sequencing Grade Modified Trypsin	Promega	Cat#V5111
Sodium orthovanadate	Merck Life Science, SLU	Cat#5086050004
Proteinase K solution	ThermoFisher	Cat# 25530049
Critical Commercial Assays		
MiR05-Kit	Oroboros Instruments	Cat#60101-01
Deposited Data		
A transmitochondrial sodium gradient controls membrane potential in mammalian mitochondria	Mendeley Data	DOI: https://doi.org/10.17632/px9537y5f9.1
Experimental Models: Cell Lines		
Wild type mouse mitochondrial cybrid FBALB/c (WT)	Laboratory of Dr. José Antonio Enríquez	N/A

(*Continued on next page*)

Continued

REAGENT or RESOURCE	SOURCE	IDENTIFIER
ND6 knock-down mouse mitochondrial cybrid FBALB/c ($ND6^{KD}$)	Laboratory of Dr. José Antonio Enríquez	N/A
ND6 knock-out mouse mitochondrial cybrid FBALB/c ($ND6^{KO}$)	Laboratory of Dr. José Antonio Enríquez	N/A
ND4 knock-out mouse mitochondrial cybrid FBALB/c ($ND4^{KO}$)	Laboratory of Dr. José Antonio Enríquez	N/A
NDUFS4 wild type mouse adult fibroblasts ($NDUFS4^{WT}$)	Laboratory of Dr. José Antonio Enríquez	N/A
NDUFS4 knock-out mouse adult fibroblasts ($NDUFS4^{KO}$)	Laboratory of Dr. José Antonio Enríquez	N/A
NDUFB11 wild type mouse adult fibroblasts ($NDUFB11^{WT}$)	Laboratory of Dr. Aleksandra Trifunovic	N/A
NDUFB11 knock-out mouse adult fibroblasts ($NDUFB11^{KO}$)	Laboratory of Dr. Aleksandra Trifunovic	N/A
Wild type human mitochondrial cybrid (hWT)	Laboratory of Dr. José Antonio Enríquez	N/A
G11778A LHON human mitochondrial cybrid (LHON)	Laboratory of Dr. José Antonio Enríquez	N/A
Experimental Models: Organisms/Strains		
B6.129S4-*Ndufs4*$^{tm1.1Rpa}$/J	Laboratory of Dr. David Sancho	Strain#027058; RRID: IMSR_JAX:027058
Recombinant DNA		
pCMV CEPIA2mt	Laboratory of Israel Sekler	Addgene plasmid # 58218
pCMV mito-sypHer	Laboratory of Jorgina Satrústegui	Addgene plasmid # 48251
pCMV GEM-GECO1	Laboratory of Jorgina Satrústegui	Addgene plasmid # 32442
Software and Algorithms		
ImageJ	doi: https://doi.org/10.1038/nmeth.2089	https://imagej.nih.gov/ij/; RRID: SCR_003070
SpectraManager v2	JASCO	https://jascoinc.com/products/spectroscopy/circular-dichroism/software/spectra-manager/
Prism8	Graph Pad Software	http://www.graphpad.com/; RRID: SCR_002798
DatLab8	Oroboros Instruments	https://www.oroboros.at/index.php/product/datlab/
Limma v-3.50.3	Bioconductor R-package	DOI: https://doi.org/10.1093/nar/gks042
Pymol	Schrödinger	http://www.pymol.org/pymol

EXPERIMENTAL MODEL AND STUDY PARTICIPANT DETAILS

Animal models

Mice were kept in standard housing conditions in a specific pathogen free (SPF) status facility on a 12-hour light/dark cycle at 20-24°C and relative humidity at 45-65%. The maintenance conditions are checked and registered daily. All animal procedures conformed to EU Directive 86/609/EEC and Recommendation 2007/526/EC regarding the protection of animals used for experimental and other scientific purposes, enforced in Spanish law under RD 1201/2005 and RD 53/2013. Mice received ad libitum food and water (5K67 LabDiet) and the number of mice per cage is limited and adapted to RD 53/2013. Experiments were carried out with males and females indistinctively at 8 weeks of age. Mice with C57BL/6J nuclear background were purchased from The Jackson Laboratory and $NDUFS4^{KO}$ mouse strain (B6.129S4-Ndufs4tm1Rpa/J) was kindly donated by Dr. David Sancho.

Cell culture and treatment

Mouse WT, CI^{KD}, CI^{KO} and $ND4^{KO}$ cybrids were generated in the lab as described elsewhere.[24] All of mouse cybrids cell lines harbor the nuclear background of L929 cells (ATCC- CCL-1) derived from Mouse C3H/An connective tissue and established in 1948. CI^{KD} carries a frameshift mutation (13887iC) that created a stop codon 51 to 53 bp downstream of a 6-C stretch within the *mt-ND6* gene, resulting in a 79-amino-acid truncated polypeptide. CI^{KO} consisted of the deletion of an A in a track of 7 As at position 10227 in the *mt-ND6* gene. This mutation led to a truncated polypeptide of only 26 amino acids.[24] WT were generated with untreated cells and following the same protocol for cybrid generation. hWT and 11778G>A mtDNA point mutation in ND4 (LHON) cybrids were generated by following the protocol for transmitochondrial cybrid generation on 143B cell nuclear background (143B is a mixed cell that was isolated from the bone of a 13-year-old, white female with osteosarcoma) and mitochondria from either healthy individuals or healthy patients and kindly donated by Dr. Raquel Moreno-Loshuertos. $NDUFS4^{WT}$ and $NDUFS4^{KO}$ were generated from $NDUFS4^{WT}$ or $NDUFS4^{KO}$ 8-week adult C57BL6/J mouse, respectively. $NDUFB11^{WT}$ and $NDUFB11^{KO}$ were derived cell lines from C57BL6/N mouse kindly donated by Dr. Alexandra Trifunovic. Since both mouse and human cell lines were harboring a nuclear background from immortalized cells (L929 and 143B, respectively) and repopulated with wild type or mutant mtDNA from different donors, ancestry, sex, race and ethnicity have not relevant meaning regarding these models.

WT, CI^{KD}, CI^{KO}, $ND4^{KO}$, hWT and LHON cybrid cells, and $NDUFS4^{WT}$ and $NDUFS4^{KO}$ mouse adult fibroblasts (MAFs), and $NDUFB11^{WT}$ and $NDUFB11^{KO}$ mouse embryonic fibroblasts (MEFs), were cultured in DMEM supplemented with 5% FBS, 100 U/mL penicillin, and 100 μg/mL streptomycin. All cells were correctly identified by proteomic analysis, CI assembly assessed by Blue Native polyacrylamide gel electrophoresis (BN-PAGE), and CI spectrophotometric activity. Chronic rotenone (Chronic Rot) treatment consisted of incubating WT cybrids with 250 nM rotenone for 4-6 hours. This rotenone concentration was maintained throughout the detachment procedure in all buffers (trypsin and PBS) until the cell pellet was placed on ice, since removing rotenone or increasing its content during detachment was found to uncouple mitochondria. All cultures were routinely checked for mycoplasma contamination and tested negative.

METHOD DETAILS

Mitochondria isolation

Mitochondria were isolated from cybrids, MAFs, or mouse heart using a protocol adapted for either cell culture or mouse tissues.[34] Briefly, hearts and liver were cleaned of blood by rinsing in ice-cold phosphate buffered solution (PBS), and the tissue was disrupted with a blade on ice. Disrupted tissue, cybrids, or MAFs were resuspended in a buffer containing 0.32 M sucrose, 10 mM Tris-base and 1 mM EDTA (pH 7.4), placed in a glass Elvehjem potter, and homogenized by up and down strokes using a motor-driven Teflon pestle. Successive homogenization–centrifugation steps yielded the mitochondria-containing fraction, which was quantified with the Bradford protein assay.

Mitochondrial membrane isolation and measurement of complex activities

Mitochondrial membranes from cultured cells or liver were obtained after freeze–thawing isolated mitochondria, and OXPHOS enzyme activity was measured as previously described,[35] using between 0.5 and 20 μg protein per sample, depending on the activity to be measured. Rotenone-sensitive NADH-ubiquinone decylubiquinone (decyl-CoQ) oxidoreduction (CI activity) was measured by changes in absorbance at 340 nm. Antimycin A-sensitive succinate-cyt c oxidoreductase activity (CII + CIII activity) was calculated after measuring changes in absorbance at 550 nm. Potassium cyanide (KCN)-sensitive cyt c-oxygen oxidoreductase activity (CIV activity) was calculated after measuring changes in absorbance at 550 nm. Oligomycin-sensitive ATPase activity (CV activity) was calculated after measuring changes in absorbance at 340 nm driven by the pyruvate kinase reaction coupled to ADP phosphorylation by CV.

Measurement of O_2 consumption and mitochondrial membrane potential

Measurements were made with an O2k Oxygraph instrument (Oroboros Instruments) with the attached fluorescent module. Tetramethylrhodamine methyl ester (TMRM) in quenching mode (2 μM) was used for the detection of mitochondrial membrane potential. Oxygen and TMRM calibration were performed before every experiment. Cells ($2x10^6$) or isolated mitochondria or mitochondrial membranes (50 μg) were loaded in the O2k Oxygraph chambers with Mir05 buffer (Oroboros Instruments) and 20 μg digitonin (only for cells); substrates and inhibitors were added sequentially. Sodium glutamate (10 mM) and malate (0.5 mM) were added to activate CI-dependent respiration and rotenone (0.5 μM) was added to suppress it. Sodium succinate (10 mM) was then added to activate CII-dependent respiration, and subsequently 1 mM ADP was added to activate state 3 respiration; both of which were inhibited by adding 2.5 μM antimycin A. Lastly, 0.5 mM N, N, N′, N′-tetramethyl-p-phenylenediamine (TMPD) and 2 mM ascorbate were added to activate CIV-dependent respiration, which was later suppressed by addition of 100 mM sodium azide. In some experiments, 10 μM cyt c was included in the sequence. In some other experiments, 100 nM nigericin or 100 nM monensin was added after succinate.

Na^+-containing respiration buffer was prepared by replacing potassium phosphate with sodium phosphate in the Mir05 formula (Oroboros instruments). Na^+-free respiration buffer was made with phosphoric acid and buffered to physiological pH with N-methyl D-glucamine (NMDG). Both buffers were compensated in osmolality and ionic strength using NMDG. In addition, in these

experiments the acidic forms of substrates, appropriately resuspended in Na^+-free respiration solution and buffered to reach respiration solution pH, were used to avoid the introduction of Na^+ into the Na^+-free respiration buffer or additional Na^+ into the Na^+-containing buffer.

Prior all experiments, TMRM was calibrated by sequentially adding increasing concentrations of the probe up to 2 μM (final concentration). In this way, it could be possible to measure the amount of probe in and out of the mitochondria during the experiment. The numbers obtained after every treatment were introduced in the Nernst equation, in which we assumed a TMRM binding correction of 6.3,[32,36] and a mitochondrial volume of 0.6 μl/mg protein.[36]

$$\Delta\psi = 61.5\, x\, log_{10}\left(\frac{1}{6.3}\, x\, \frac{\frac{TMRM_{in}}{Mito.\ vol.}}{\frac{TMRM_{out}}{Buffer\ vol.}}\right)$$

Given that TMPD and azide absorb light in the specific wavelength used for TMRM excitation/emission, we performed a chemical background calibration in which we added the corresponding amounts of TMPD and azide in the presence of TMRM and in the absence of mitochondria. The values obtained were subtracted from the values with mitochondria. To note, given that the chemical background calibration may not yield accurate quantification of ΔΨmt, we cautiously provided CIV-dependent ΔΨmt values in a.u., not in mV.

Blue native gel electrophoresis

Complex and supercomplex levels, compositions, and distributions were analyzed in isolated mitochondria by BN-PAGE.[37] Mitochondrial proteins were solubilized with 10% digitonin (4 g/g; Sigma-Aldrich D5628) and separated on 3–13%-gradient Blue native gels. Gradient gels (1.5-mm thick) were prepared using a gradient former connected to a peristaltic pump.

SDS gel electrophoresis

Mitochondria were resuspended in RIPA buffer (1% Triton-X-100, 50 mM Tris-HCl pH 7.4, 50 mM sodium chloride, 0.5% sodium deoxycholate, and 5 mM EDTA) supplemented with a protease inhibitors cocktail mix (Sigma P8340). Samples were then incubated at 4°C on a rotating wheel for 15 minutes and centrifuged for 15 minutes at 13,000 x g at 4°C. Supernatants were collected and transferred to fresh 1.5 ml Eppendorf tubes. Protein concentration was quantified by the Bradford assay.

The levels and distribution of Opa1 were analyzed by sodium dodecyl sulphate (SDS) gel electrophoresis (SDS-PAGE) on 7.5% gels. Loading buffer (50 mM Tris-HCl pH 6.8, 2% SDS, 10% glycerol, 1% 2-mercaptoethanol, 0.02% bromophenol blue) was added to samples, which were incubated for 5 minutes at 95°C.

Immunodetection of single proteins, complexes, and supercomplexes

BN-PAGE or SDS-PAGE proteins were electroblotted using a Mini Trans-Blot Cell system (Bio-Rad) onto polyvinylidene difluoride (PVDF) transfer membrane (Immobilon-FL, 0.45 μm; Merck Millipore, IPFL00010) for 1 hour at 100 V in transfer buffer (48 mM Tris, 39 mM glycine, and 20% ethanol). Non-specific binding sites were blocked by incubating membranes with phosphate-buffered saline (PBS) containing 5% bovine serum albumin (BSA) for 1 hour at RT. For protein detection, membranes were incubated in blocking buffer containing primary antibody overnight at 4°C. After three washes with PBS 0.1 % Tween-20 (PBS-T) for 30 min, membranes were incubated with appropriate secondary antibodies for 1 hour at RT. Membranes were then washed twice with PBS-T and once with PBS. To study CI proteoliposome orientation, the PVDF membrane was incubated with one antibody against CI P module (anti-NDUFB7, Proteintech, 14912-1-AP) and another one against CI N module (anti-NDUFV2, Abcam, ab183717). To study complex and supercomplex assembly, the PVDF membrane was sequentially probed with antibodies against CI (anti-NDUFA9, Abcam ab14713), CIII (anti-UQCR2, Proteintech, 14742-1 AP) and CII (anti-Fp70, Invitrogen, 459200). Parallel BNGE western blots were performed to probe CIV (anti-COI, Invitrogen, MTCO1 459600) and CV (anti-ATPβ, Abcam, Ab 14730). To study Opa1 processing, the PVDF membrane was sequentially probed with antibodies against Opa1 (anti-Opa1, Abcam, ab42364) and SDHA (anti-Fp70, Invitrogen, 459200). Fiji software was used for Opa1 quantification. Antibody binding was detected by fluorescence as previously described.[38]

Measurement of mitochondrial ATP synthesis

ATP synthesis was assessed in isolated mitochondria (1.5 to 15 μg mitochondrial protein) using succinate as substrate (plus rotenone) in the presence of ADP in a kinetic luminescence assay based on the luciferin/luciferase reaction.[39]

Measurements of mitochondrial matrix Na^+ and H^+

The probe-loading protocol was adapted from.[40] Isolated mitochondria from cells were incubated for 20 min at 37 °C with 10 μM 2',7'-bis-(2-carboxyethyl)-5-(and-6)-carboxyfluorescein-acetoxymethyl ester (BCECF-AM; for matrix H^+) or with 1,3-benzenedicarboxylic acid, 4,4'-[1,4,10-trioxa-7,13-diazacyclopentadecane-7,13-diylbis(5-methoxy-6,12-benzofurandiyl)]bis-,tetrakis [(acetyloxy) methyl] ester (SBFI-AM; for matrix Na^+). This was followed by two rounds of centrifugation (12000 g, 4°C, 5 min) and resuspension in sucrose buffer. The last resuspension was in Na^+-free respiration buffer.

Probe-loaded mitochondria were distributed in p96 wells in Na^+-free buffer, unless otherwise indicated. Measurements were made with a Fluoroskan Ascent microplate reader (Thermo Fisher Scientific) at 390/485 nm excitation pair for BCECF-AM and 355/390 nm excitation pair for SBFI-AM. Emission was recorded at 530 nm emission for BCECF-AM and SBFI-AM. Substrates and inhibitors were subsequently added as in the O_2 consumption experiments, without ADP, TMPD, ascorbate, or sodium azide. The H^+ pumping rate was obtained from the slope after adding respiratory substrates; the slope was flat after the addition of the corresponding inhibitors. For the measurement of reverse NHE activity using BCECF-AM, 10 mM NaCl was added after succinate. For measurement of forward NHE activity and Na^+ gradient using SBFI-AM, 10 mM NaCl was added at the beginning of the experiment.

Calibration was performed by adding equal amounts of mitochondria from the same cell type to several wells containing a graded series of pH or Na^+ concentration in the presence of 1 μM nigericin, 1 μM monensin, and 1 μM gramicidin.

Spectrophotometric swelling assay in isolated mitochondria

The protocol was adapted to the analysis of cell-culture-derived mitochondria from Douglas and Cockrell.[15] Briefly, passive mitochondrial swelling was recorded in 50 μg of mitochondria resuspended in 133 mM sodium acetate (for NHE activity), potassium acetate (for KHE activity) or ammonium aceate (for maximal swelling), 0.2 mM Tris-EGTA, pH 7.0 at room temperature. Absorbance was recorded at 550 nm in a UV/VISJASCO spectrophotometer (Thermo Fisher Scientific).

In some experiments, sodium acetate was exchanged for sodium chloride as a swelling control. In others, before addition of mitochondria to the sodium acetate buffer, mitochondrial CI was activated by incubating the sample with glutamate/malate in Miro05 buffer for 5 min at 37°C. Alternatively, mitochondrial CI was deactivated by incubating the mitochondria without substrates in Miro05 buffer for 15 min at 37°C.

Measurement of Na^+ gradient in whole cells by confocal microscopy

Cytosolic and mitochondrial Na^+ were detected as in Hernansanz-Agustín et al.[38] Briefly, cybrids were plated the day before experiments, washed three times with Hank's balanced salt solution with Ca^{2+}/Mg^{2+}/glucose (HBSS + Ca/Mg + glucose), and incubated with 5 μM Asante NaTRIUM Green-2-Acteoxymethyl ester (ANG2-AM) for 30 min at 37 °C in the dark. ANG2-AM was washed out, and new HBSS + Ca/Mg + glucose was added, including 1 μM CoroNa Red. Cells were further incubated for 30 min at 37 °C in the dark. After this, the medium was changed again, cells were washed once with HBSS + Ca/Mg + glucose, and the plate was placed on the automated stage of a Leica SP-5 confocal microscope for live imaging. The planes were focused for image capture, and images were taken with a ×63 objective. Experiments started and ended at 20% O_2 and 5% CO_2. Loaded cells were excited with an argon/krypton laser using the 496-nm line for ANG2-AM and the 514-nm line for CoroNa Red. Fluorescence emission of ANG2-AM was detected in the 515–550-nm range, whereas the emission of CoroNa Red was detected in the 555–575-nm range.

In situ calibration of the same cells was performed after a two-wash step with Na^+-free HBSS + Ca/Mg + glucose. Increasing Na^+ concentrations, starting from 0 mM Na^+, were then applied in the presence of 1 μM nigericin, 1 μM monensin, and 1 μM gramicidin, and images were taken with the excitation/emission wavelengths indicated above. Calibration solutions were equilibrated for at least 5 min.

Measurement of mitochondrial Ca^{2+} and pH, and cytosolic Ca^{2+} in whole cells by confocal microscopy

The protocol followed was exactly as in Hernansanz-Agustín et al.[38] Briefly, cells were transiently transfected with Cepia2mt (for mitochondrial Ca^{2+}), mitosypHer (for mitochondrial pH) or cytoGECO (for cytosolic Ca^{2+}) and were all imaged under a Leica SP5 microscope. Cellular and mitochondrial Ca^{2+} entry was stimulated by addition of Histamine 100 μM and calibrated using ionomycin 2 μM and EDTA 10 mM. pH calibration was performed with HBSS + Ca/Mg + glucose + monensin 1 μM, nigericin 1 μM and gramicidin 1 μM at different pHs.

Measurement of ΔΨmt in whole cells by confocal microscopy

Cells were seeded the day prior experimentation. Then, cells were incubated with TMRM 50 nM, for non-quenching mode, for 30 min before imaging in a Leica SP5 microscope. Samples were excited with an argon/krypton laser using the 543-nm line and emission was detected in the 555–595-nm range. Calibration was performed following guidelines and indications published elsewhere.[41] Briefly, TMRM signal was measured in and out of mitochondria before and after addition of 1 μM FCCP. FCCP-corrected values were introduced in the Nernst equation. TMRM binding correction and mitochondrial volume were assumed as above and the cell volume was estimated as 80 μl/mg protein.[42]

$$\Delta\psi = 61.5\ x\ log_{10}\left(\frac{1}{6.3}\ x\ \frac{\frac{TMRM_{in}}{Mito.\ vol.}}{\frac{TMRM_{out}}{Cell\ vol.}}\right)$$

Measurement of mitochondrial volume

For the determination of mitochondrial volume 50 μg of mitochondria and 1 mL Mir05 respiration buffer were placed in a cuvette, and the absorbance at 550 nm was recorded with a UV/VISJASCO spectrophotometer (Thermo Fisher Scientific). Parallel measurements were

taken at steady state and in mitochondria respiring from different substrates for 5 min at 37 °C. A valinomycin technical control was included to determine whether this technique was suitable for the measurement of mitochondrial volume changes, with positive results.

Transmission electron microscopy

Cells were fixed for 1 hr at 25°C using glutaraldehyde dissolved in EB at a final concentration of 1.25%, embedded in plastic, sectioned, and stained with uranyl acetate and lead citrate. Images Cells were analysed by electron microscopy as previously described.[38] Briefly, for fields of mitochondria at least four different transmission EM micrographs representing different areas in the grid and cells were selected. Thin sections including mitochondria were imaged with a JEM1010 electron microscope (Jeol).

LHON mutation structural modelling

Molecular scheme represented in Video S1 developed with pymol.

Proteomic analysis

Protein extracts of whole cells or isolated mitochondria from WT, ND6^{KD}, ND4^{KO}, NDUFS4^{WT}, NDUFS4^{KO}, hWT, LHON or pure CI samples were obtained by homogenization with ceramic beads (MagNa Lyser Green Beads, Roche, Germany) in CS buffer (Pipes pH6.8, MgCl2, NaCl, EDTA, sucrose, SDS, sodium orthovanadate; Biochain Institute, Inc. #K3013010-5) freshly supplemented with protease and phosphatase inhibitors. Extracted proteins (around 200 μg) were subjected to in-filter reduction and alkylation using iodoacetamide followed by trypsin digestion (Nanosep Centrifugal Devices with Omega Membrane-10K, PALL), and the resulting peptides were TMT-labeled according to the manufacturer's instructions. Labeled peptides were loaded and washed on Evotips for chromatographic separation by an evosep one HPLC system (30 SPD method, with Endurance Column 15 cm x 150 μm ID, 1.9 μm beads-EV1106, Evosep). Mass spectra were acquired in a data-dependent manner, with an automatic switch between MS and MS/MS using a top-speed method and dynamic exclusion. MS spectra were collected in the Orbitrap analyser using a mass range of 375–1500 m/z at 60,000 resolution. HCD fragmentation was performed at 33 eV of normalized collision energy and MS/MS spectra were analysed at 30,000 resolution in the Orbitrap.

Proteins were identified with the SEQUEST HT algorithm integrated in Proteome Discoverer 2.5 (Thermo Scientific). MS/MS scans were searched against a pig reference target-decoy protein database (human_pig_202105_pro-sw-tr.target-decoy.fasta), (296316 sequences in total). For database searching, parameters were selected as follows: trypsin digestion with 2 maximum missed cleavage sites, precursor mass tolerance of 2 Da, and a fragment mass tolerance of 0.03 Da. Methionine oxidation (+15.994915 Da) and asparagine and glutamine deamidation (+0.984016 Da) were set as variable modifications, whereas cysteine carbamidomethylation (+57.021464 Da) and TMT labeling (+229.162932 Da) at peptide N-terminal ends and Lys residues were considered fixed modifications. False discovery rates (FDR) for peptide identifications were calculated by the refined method[43] after additional filtering for a precursor mass tolerance of 10 ppm.[44] A 1% FDR was used as criterion for peptide identification. Proteins showing differential expression between WT and KO were identified using limma v-3.50.3 (refence 1) based on Zq values.

Quantitative information from TMT reporter intensities was integrated from the spectrum level to the peptide level and then to the protein level based on the WSPP model,[45,46] using the GIA integration algorithm.[47]

To note, taking into account that the protein extraction protocol is not specific for membrane proteins, the peptides of these proteins are poorly represented in this study. This includes ND6 or ND4 in all models analyzed.

Purification of Porcine Heart Complex I

Intact mitochondria were isolated from fresh homogenizedin 0.25 M sucrose, 10 mM Tris-HCl (pH 7.4) and washed twice in the same medium before fragmentation as previously described.[48] The pellet was resuspended in 50 mM TrisHCl (pH 8.0), 20% (v/v) glycerol, frozen in liquid nitrogen, and stored at -80°C. The Complex I was purified using an adapted multiple column strategy as described by Letts et al.[49] alternating anion exchange with buffer A (20 mM Tris-HCl, pH 7.4, 10% (v/v) glycerol, 1 mM EDTA, 1 mM DTT, 0.1 mg/ml POPC, and 0.1 % DDM) and buffer B(20 mM Tris-HCl, pH 7.4, 10% (v/v) glycerol, 1 mM EDTA, 1 mM DTT, 0.1 mg/ml POPC, and 0.1 % DDM, 1M NaCl) followed by size exclusion chromatography (SEC) using the SEC buffer (20 mM HEPES, pH 7.4, 2 mM EDTA, 10% glycerol, 50 mM NaCl, 0.1 mg/ml POPC/CL (4:1) and 0.05% DDM).

Briefly, to solubilize complex I from the mitochondrial membranes DDM (10% w/v) was added to dropwise to a final concentration of 1% DDM and incubated for 30 minutes on an orbital shaker at 4 °C. To remove the non-solubilized material samples were centrifuged at 80,000 × g for 20 min (Beckman MLA80 rotor, Optima-MAX XP ultracentrifuge).

Next, the obtained Supernatant was filtered (0.45 μm pore size) and loaded onto 20-ml Mono Q HR anion-exchange column (GE Healthcare) previously equilibrated with equilibration buffer (20 mM Tris-HCl, pH 7.4, 10% (v/v) glycerol, 1 mM EDTA, 1 mM DTT, 0.1 mg/ml POPC, and 0.1 % DDM, 50 mM NaCl). After the application of the mitochondrial extract, the Mono Q column was washed with 11 ml of 5% buffer B, followed with a 11-ml linear gradient of 5 - 23% buffer B, and finally with 68 ml of 23% buffer B. Complex I was then eluted with a 89-ml linear gradient of 23–30% buffer B followed with 40 ml of 100% buffer B to elute any protein from the column. The Q-Sepharose gradient was run at 1.0 ml/min at 4 °C. Complex I containing fractions were pooled based on NADH/FeCy activity and concentrated with centriprep-10 K Centrifugal Filters (Milipore) to a final volume of 10 ml. This sample was loaded onto a Hiprep 26/60 Sephacryl S 300 HR column (GE Healthcare) equilibrated with SEC buffer and eluted overnight at 0.35 ml/min at 4 °C.

Complex I containing fractions were identified by spectrophotometrically CI activity and BN-PAGE, followed by CI in-gel activity.

Reconstitution of Complex I into proteoliposomes

The fraction chosen for reconstitution was the corresponding to the CI in-gel activity BN-PAGE band which showed more CI abundancy and a specific activity band at the level of CI (fraction 10). This fraction was also analyzed by mass spectrometry to confirm CI purity. Purified Complex I was reconstituted into proteoliposomes using the rapid detergent dilution method.[50] For this purpose, 100 μl of solubilized Complex I (0.2 mg/mL) was mixed with 20 μl of synthetic POPC/CL (4:1 w/w; 20 mg/mL) and incubated for 30 min on ice. Subsequently, the mixture was diluted by the addition of 4 ml of reconstitution buffer (50 mM Tris-HCl, pH 7,4) and left on ice for additional 20 min. Complex I-containing proteoliposomes were collected by high-speed centrifugation (30 min; 400000 g; 4°C) and resuspended in 100 μl (initial volume of the purified Complex I) of reconstitution buffer. The reconstituted CI proteoliposomes were aliquoted and used for further experiments.

CI orientation within proteoliposomes was measured by incubating the proteoliposomes with proteinase K for 10, 30, 60, 150, 300, 600 and 1200 seconds on ice, in Tris-HCl 30 mM, pH 8.0 buffer. Then, phenylmethylsulfonyl fluoride (PMSF) 5 mM was used to inactivate the protease and samples were diluted to run SDS electrophoresis.

Measurement of Pure Complex I NHE activity and membrane potential into proteoliposomes

CI-containing proteoliposomes were either reconstituted with acridine orange (AO; 10 μM) or only buffer. Proteoliposomes with AO were incubated for 5 min in reconstitution buffer, measurement started once the plate reached 37°C and NaCl 30 mM was added during the measurement. Measurements were made with a Fluoroskan Ascent microplate reader (Thermo Fisher Scientific) at 495/525 nm excitation/emission filter pair. Unloaded proteoliposomes or liposomes alone were added to the preheated reconstitution solution containing 30 mM NaCl and either 10 μM of SBFI or 10 μM BCECF and, where indicated, the corresponding inhibitors during the fluorometric measurement. For measurements of membrane potential, unloaded proteoliposomes or liposomes alone were mixed with 2 μM of TMRM and 130 μM decylUb in reconstitution solution in the absence of presence of 30 mM NaCl. TMRM fluorescence was recorded before and after the addition of 100 μM NADH. Measurements were made with a Fluoroskan Ascent microplate reader (Thermo Fisher Scientific) at 390/485 nm excitation pair for BCECF, 355/390 nm excitation pair for SBFI and 545 nm for TMRM. Emission was recorded at 530 nm emission for BCECF and SBFI, and 580 for TMRM. Membrane potential created by energized proteoliposomes was sensitive to FCCP or low dose rotenone treatment. SBFI calibration was performed by acquiring its fluorescence in a solution with minimal (approximately 0 mM Na^+) and saturated (238 mM Na^+) Na^+ solutions in the presence of proteoliposomes. BCECF calibration was performed by measuring its fluorescent signal at a lower and a higher pH, typically pH 6.5 and pH 8.5. For hWT and LHON proteoliposomes, pH and TMRM signals were relativized to their respective NADH:CoQ oxidoreductase activities.

Analysis of mitochondrial morphology by confocal microscopy

Glass cover slips were consecutively washed with 100% EtOH and PBS 1x and irradiated with UV light for 20 min to sterilize them. Once dry, one cover slip was placed per well on a P12 cell culture plate. 30,000 cells were plated per well in complete DMEM and were left incubating at 37°C overnight. The following day, cells were incubated for 20 min at 37°C in DMEM containing 33 nM Mitotracker® Deep Red FM, after which the medium was discarded and exchanged for fresh DMEM in which the cells remained for 2 h at 37°C. Finally, cells were fixed in 4% PFA for 15 min at 37°C, followed by three washes in PBS 1x. Cells were stained with DAPI (1:1000) and mounted using ProLong® Gold Antifade Reagent (Invitrogen). Confocal fluorescence microscopy images were obtained at a Leica SP5 inverted confocal microscope using HCX PL APO lambda blue 63x 1.40 oil objectives and a digital zoom of 2x. Z-stack images (step size: 0.35 μm) were acquired with LAS-AF 2.6.0 software (Leica Microsystems).

Image analysis was performed in FIJI 1.53t using the Mitochondria Analyzer plugin.[51] Maximum projection images of Mitotracker signal were thresholded with the 2D Batch Analysis function with the following parameters: subtract background (rolling: 2.0), sigma filter plus (2.0 radius), enhance local contrast (max slope: 3.0), weighted mean threshold (block size: 1.0, C-value: 5.0), despeckle and remove outliers (pixels: 4.0). Individual cells were isolated from whole thresholded images, and size parameter of mitochondria were calculated on a per cell basis.

Measurement of H^+ movement by electrophysiology

Measurements were made in an O2k Oxygraph instrument (Oroboros Instruments) with the attached pH electrode module. Isolated intact mitochondria (100 μg), liposomes (100 μl) or CI-containing proteoliposomes (100 μl) were loaded in the O2k Oxygraph chambers with a low-buffering capacity buffer (2 mM imidazole, 140.66 mM KCl 140.66 mM, 0.49 $MgCl_2$ and 0.1 mM EDTA, pH 7.1 (adjusted at 25° C). pH electrode was calibrated in the day of the experiment and the buffer pH recorded before and after the addition of 30 mM NaCl.

Measurement of isolated and NHE-linked mitochondrial channel activities

NHE-linked NCLX, MCU and TMBIM5 activities were assessed as previously described.[52] Briefly, isolated mitochondria were added to a Ca^{2+}-free, respiratory buffer containing 10 mM succinate, 1 μM rotenone, 4 mM ADP and 10 μM Calcium Green (Invitrogen). NHE-linked NCLX and MCU activities were done in the presence of 10 mM Na^+, whereas TMBIM5 activity was done in its absence. A 50 μM $CaCl_2$ bolus was added to the solution and mitochondrial Ca^{2+} entry was monitored until it reached basal values again, then

1 μM Ru360 was added to inhibit MCU and mitochondrial Ca^{2+} exit was followed. Samples were excited using a 485 nm filter and emission was recorded using a 515 nm filter in a Fluoroskan Ascent microplate reader (Thermo Fisher Scientific).

We assessed isolated NCLX activity previously published,[53] with some changes. Briefly, isolated mitochondria were loaded with 10 μM Fluo4-AM following the same protocol as for SBFI-AM and BCECF-AM (see above). Next, 50 μg of mitochondria were loaded into a Ca^{2+} free buffer and a bolus of 50 μM $CaCl_2$ was added. After Ca^{2+} stabilization with the mitochondria, Na^+ was added and the slope of Ca^{2+} exit recorded. Samples were excited using a 485 nm filter and emission was recorded using a 515 nm filter in a Fluoroskan Ascent microplate reader (Thermo Fisher Scientific).

QUANTIFICATION AND STATISTICAL ANALYSIS

Statistical analyses and graphics were produced with GraphPad Prism 8 software. Datasets were compared by t test, analysis of variance (ANOVA), or nonparametric analysis as appropriate and with P values adjusted for multiple tests. P values from each comparison are shown in every graph. All results are presented as mean ± SD or mean ± SEM.

CellPress
OPEN ACCESS

Supplemental figures

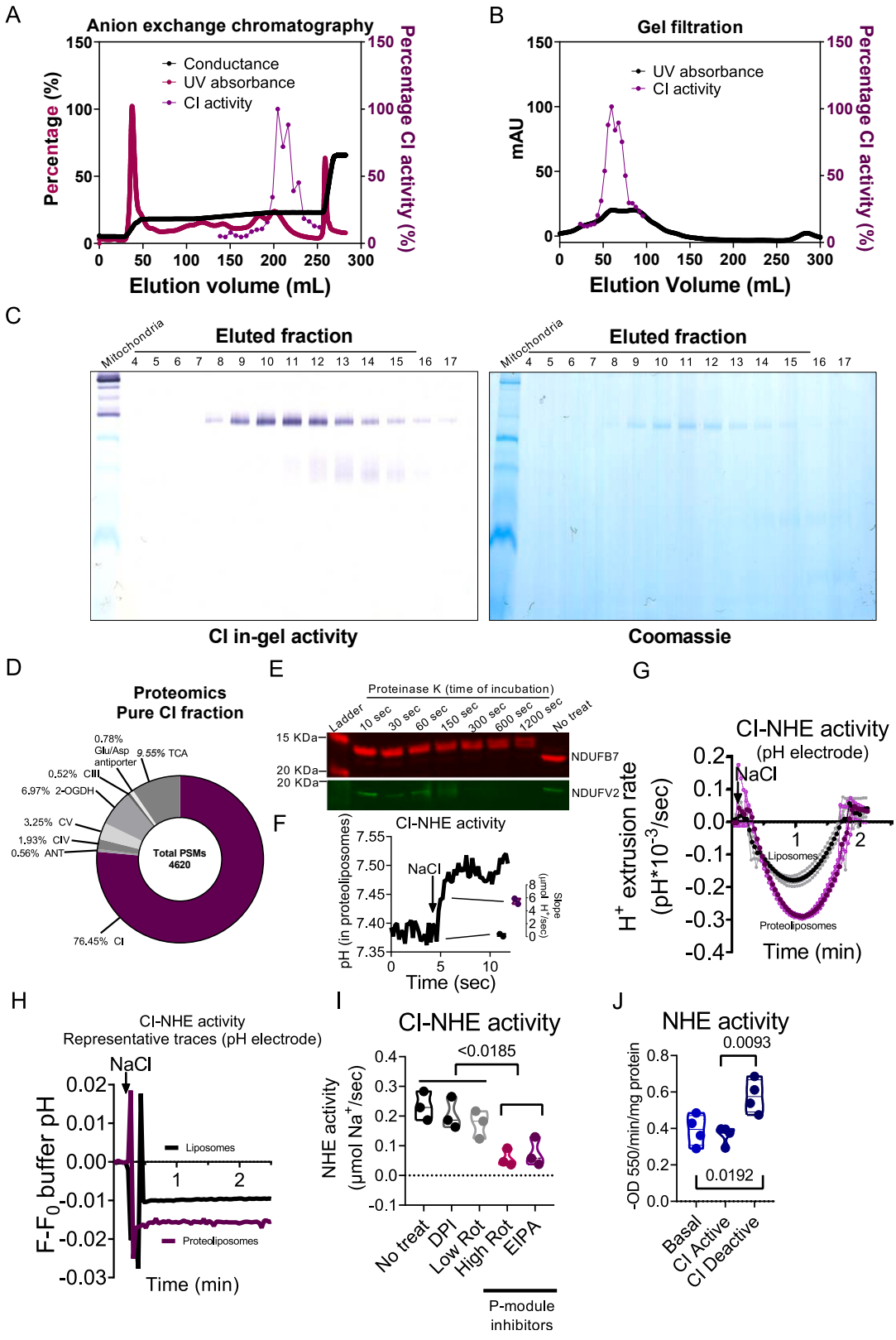

(legend on next page)

Figure S1. Pure CI reconstituted into proteoliposomes is a Na+/H+ antiporter, related to Figure 1

(A) Anion exchange chromatography profile showing the percentage of conductance, UV absorbance, and CI activity.

(B) Gel filtration profile showing the UV absorbance and percentage of CI activity of the samples previously enriched by anion exchange chromatography.

(C) BN-PAGE CI in-gel activity (left) and Coomassie staining (right) of the eluted fractions from the gel filtration containing CI. Isolated pig heart mitochondria were loaded as a control to corroborate sole migration of CI in the eluted fractions.

(D) Proteomic analysis of the fraction used for proteoliposome reconstitution.

(E) Western blot showing CI P-module (NDUFB7) or N-module (NDUFV2) proteoliposome susceptibility to proteinase K incubation.

(F) Representative trace of fluorescence of CI-containing proteoliposomes loaded with 10 μM BCECF was measured before and after the addition of NaCl 10 mM to test forward NHE. Inset shows the quantification of two independent experiments.

(G) Buffer pH was measured with a pH electrode in a solution containing CI-containing proteoliposomes or liposomes before and after the addition of NaCl 30 mM to test forward NHE (n = 4). Semi-transparent lines represent each replicate and the opaque line the mean of all experiments.

(H) Representative raw traces of buffer pH from (F).

(I) Buffer Na^+ content was measured before and after the addition of pure CI-containing proteoliposomes in the absence ("no treat") or presence of 1 μM diphenyleneiodonium (DPI), 1 μM rotenone (low Rot), 100 μM rotenone (high Rot), or 10 μM 5-(N-ethyl-N-isopropyl)amiloride (EIPA) to test forward NHE. CI substrates were not added in the mixture (n = 3).

(J) Mouse liver mitochondrial reverse NHE activity in different CI activation states (n = 4).

Violin plots show dots representing every replicate and a dotted line indicating the mean of all experiments. p values represent two-way ANOVA (I) and one-way ANOVA (J) analyses.

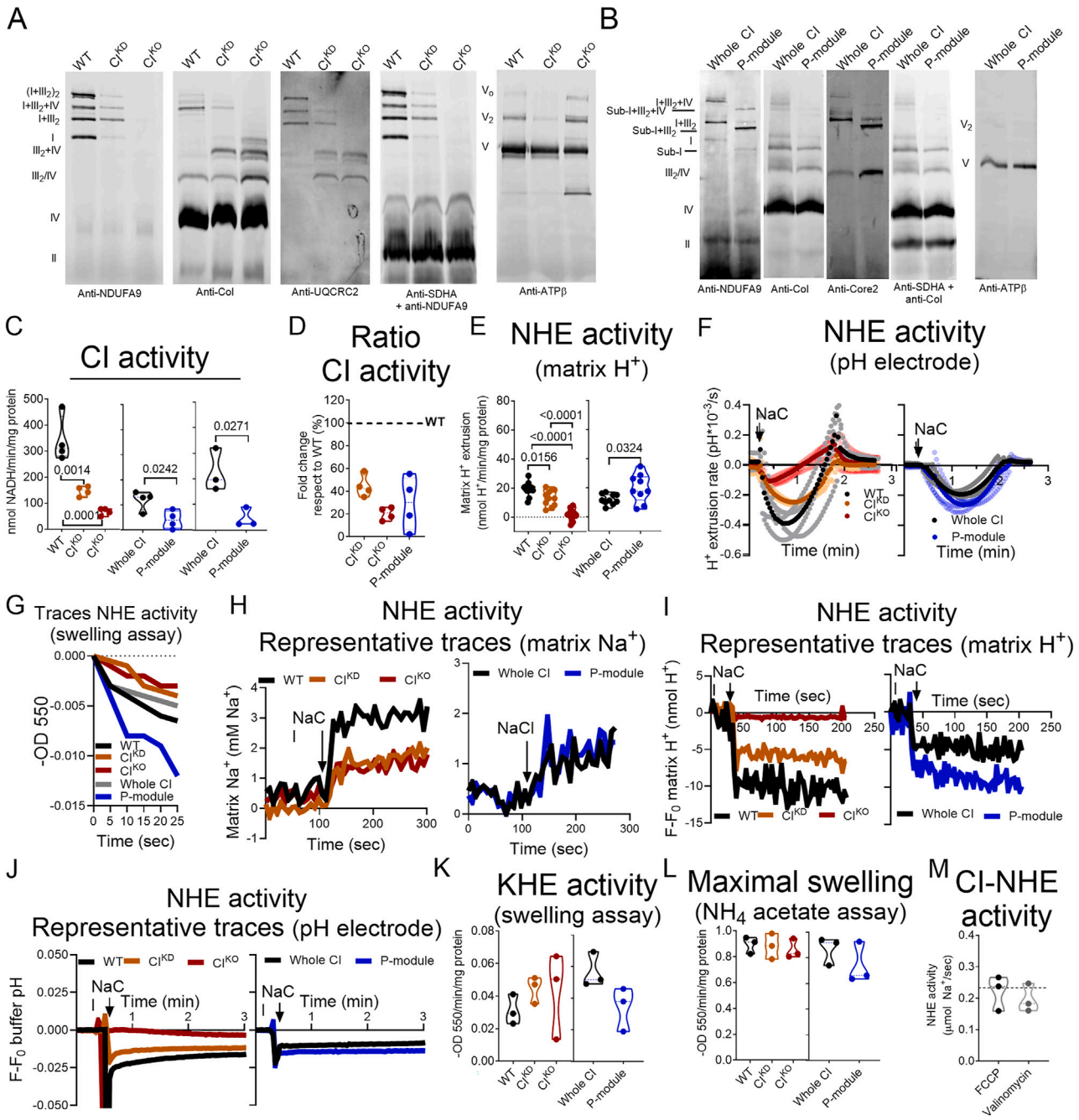

Figure S2. Differential CI subunit suppression translates into either loss or gain mNHE function, related to Figure 1

(A) Blue-native electrophoresis (BN-PAGE) of mitochondria from WT, CI^{KD}, and CI^{KO} cybrid cell lines (n = 3 per genotype) immunoblotted to detect subunits of CI (anti-NDUFA9), CIV (anti-CoI), CIII (anti-Core2), CII (anti-SDHA), and CV (anti-ATPβ). * marks an unspecific band.

(B) BN-PAGE of mitochondria from NDUFS4^{WT} (whole CI) and NDUFS4^{KO} (P-module) mouse adult fibroblasts (MAFs) (n = 2) blotted against the same epitopes as in (A). The lateral labels in (A) and (B) indicate the migrated positions of all detected complexes and supercomplexes.

(C) Rotenone-sensitive NADH-decylCoQ oxidoreductase activity in WT, CI^{KD}, CI^{KO} (left panel), Whole CI and P-module (MAFs in central and liver in right panel) mitochondrial membranes (n = 4). p values represent one-way ANOVA and t test analyses.

(D) Ratio of the CI activity of CI^{KD}, CI^{KO}, and NDUFS4^{KO} (P-module) with respect their isogenic control (n = 4).

(E) Mitochondrial matrix H^+ extrusion measured with BCECF-AM in WT, CI^{KD}, CI^{KO}, NDUFS4^{WT} (whole CI), and NDUFS4^{KO} (P-module) intact mitochondria respiring on succinate and 1 µM rotenone to test reverse NHE (n = 11; n = 10 in whole CI and n = 9 in P-module). p values represent one-way ANOVA (left) and t test (right) analyses.

(legend continued on next page)

(F) Buffer pH was measured with a pH electrode in a solution containing 100 μg of WT, CI^{KD}, CI^{KO}, $NDUFS4^{WT}$ (whole CI), and $NDUFS4^{KO}$ (P-module) intact mitochondria before and after the addition of NaCl 30 mM to test reverse NHE. Semi-transparent lines represent each replicate and the opaque line the mean of all experiments.
(G) Representative traces of passive reverse NHE activity swelling assay of WT, CI^{KD}, CI^{KO}, $NDUFS4^{WT}$, and $NDUFS4^{KO}$ intact mitochondria.
(H) Representative traces of mitochondrial matrix Na^+ measured with SBFI-AM in WT, CI^{KD}, CI^{KO}, $NDUFS4^{WT}$ (whole CI), and $NDUFS4^{KO}$ (P-module) intact mitochondria before and after the addition of 10 mM NaCl to test reverse NHE.
(I) Representative traces of mitochondrial matrix H^+ measured with BCECF-AM in WT, CI^{KD}, CI^{KO}, $NDUFS4^{WT}$, and $NDUFS4^{KO}$ intact mitochondria respiring on succinate and 1 μM rotenone before and after the addition of 10 mM NaCl to test reverse NHE.
(J) Representative raw traces of buffer pH from (F). Passive KHE activity swelling assay in WT, CI^{KD}, CI^{KO}, $NDUFS4^{WT}$, and $NDUFS4^{KO}$ intact mitochondria ($n = 3$).
(K) Passive KHE activity in WT, CI^{KD}, CI^{KO}, $NDUFS4^{WT}$ (whole CI), and $NDUFS4^{KO}$ (P-module) intact mitochondria was performed in NH_4 acetate buffer ($n = 3$).
(L) Maximal swelling assay in WT, CI^{KD}, CI^{KO}, $NDUFS4^{WT}$ (whole CI), and $NDUFS4^{KO}$ (P-module) intact mitochondria was performed in NH_4 acetate buffer ($n = 3$).
(M) Buffer Na^+ content was measured before and after the addition of pure CI-containing proteoliposomes in the presence of 1 μM FCCP and 1 μM valinomycin. Dotted line represents no treat mean value from Figure S1H.
Violin plots show dots representing every replicate and a dotted line indicating the mean of all experiments.

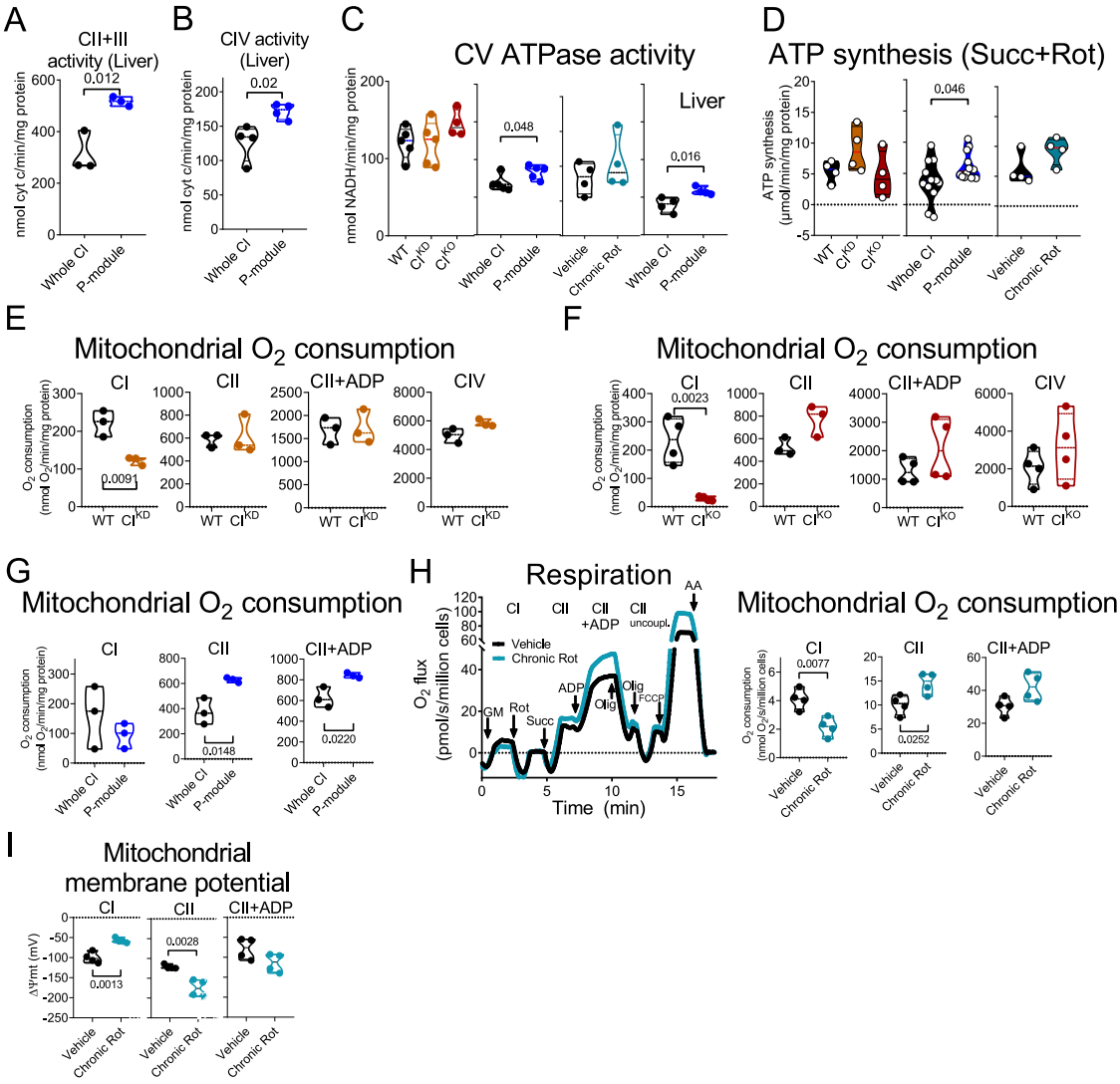

Figure S3. Bioenergetics analysis of isolated mitochondria from all CI-deficiency models, related to Figure 2

(A) Antimycin A (AA)-sensitive succinate-cyt c oxidoreductase activity in NDUFS4^{WT} (whole CI) and NDUFS4^{KO} (P-module) mouse liver mitochondrial membranes (n = 3).

(B) KCN-sensitive cyt c oxidase activity in NDUFS4^{WT} (whole CI) and NDUFS4^{KO} (P-module) mouse liver mitochondrial membranes (n = 3).

(C) Oligomycin (Olig)-sensitive ATPase activity in WT (n = 5), CI^{KD} (n = 5), CI^{KO} (n = 4), vehicle-treated (n = 4), chronic rotenone-treated (n = 4), and NDUFS4^{WT} (n = 5) and NDUFS4^{KO} (n = 5) mitochondrial membranes from MAFs and liver.

(D) Olig-sensitive ATP synthase activity in WT, CI^{KD}, CI^{KO}, vehicle-treated, chronic rotenone-treated (n = 4), and NDUFS4^{WT} (whole CI) and NDUFS4^{KO} (P-module) (n = 12) isolated mitochondria in the presence of 1 µM Rot and respiring on succinate.

(E–G) Quantification of respiratory rates of WT and CI^{KD} (E), WT and CI^{KO} (F) and NDUFS4^{WT} (whole CI) and NDUFS4^{KO} (P-module) (n = 3) (G) isolated mitochondria respiring on CI substrates (CI inset), CII substrates (CII inset), CII substrates + ADP (CII+ADP inset), and CIV substrates (CIV inset) (n = 3).

(H) (Left) Oxygen consumption rates were measured in permeabilized WT cells that had been treated with vehicle or chronic Rot (n = 4). Insets and acronyms are the same as those in Figure 2 and sections (E–G); FCCP, carbonyl cyanide-p-trifluoromethoxyphenylhydrazone (n = 4).

(I) Calibrated TMRM signal in permeabilized WT cells that had been treated with vehicle or chronic Rot, respiring on CI substrates (CI inset), CII substrates (CII inset), or CII substrates + ADP (CII+ADP inset).

Violin plots show dots representing every replicate and a dotted line indicating the mean of all experiments. p values represent t test analyses.

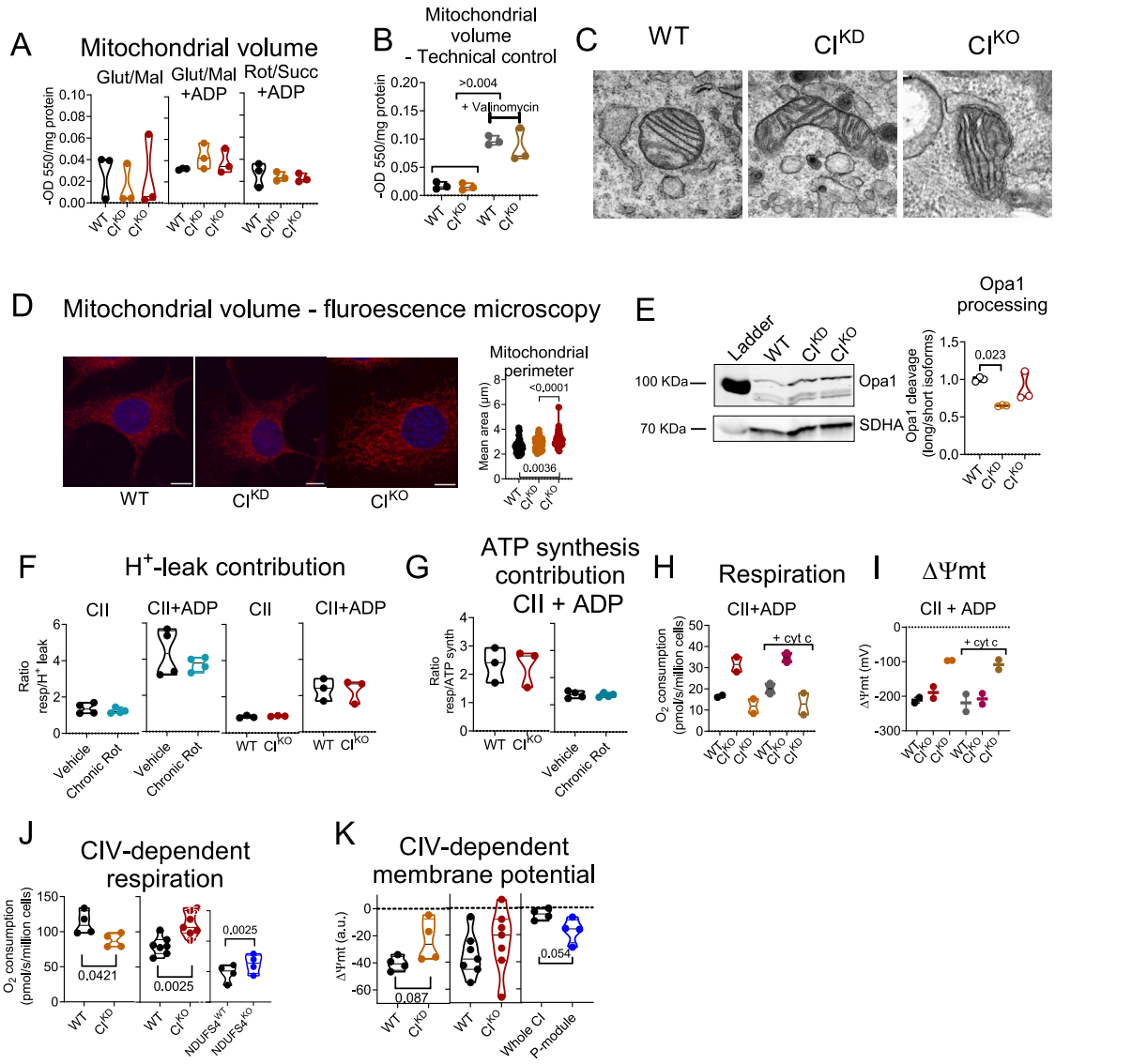

Figure S4. CI^{KD} and CI^{KO} mitochondria have similar size and membrane permeability than WT and maintain their bioenergetic footprint under CIV substrates, related to Figure 2

(A) Mitochondrial volume measured by absorbance at 550 nm in the presence of CI substrates (Glut/Mal), CI substrates + ADP (Glut/Mal+ADP), or CII substrates + 1 µM rotenone (Rot/Succ+ADP) in WT, CI^{KD}, and CI^{KO} mitochondria.

(B) WT and CI^{KD} mitochondrial volume in the absence or presence of valinomycin. *p* values represent t test analysis.

(C) Transmission electron microscopy (TEM) imaging of mitochondria in WT, CI^{KD}, and CI^{KO} cells (n = 2).

(D) MitoTracker Deep-Red and DAPI staining of WT, CI^{KD}, and CI^{KO} were analyzed by confocal microscopy. Inset: mitochondrial area was calculated with a Mitochondria Analyzer plugin (n = 37). *p* values represent one-way ANOVA analysis.

(E) Western blot analysis of OPA1 expression in WT, CI^{KD}, and CI^{KO} isolated mitochondrial fractions; anti-Fp70 was used as a loading control. Inset: shows quantification of three independent experiments. *p* values represent one-way ANOVA analysis.

(F) H$^+$ leak contribution to baseline CII respiration ± ADP in vehicle and chronic Rot-treated, as well as in WT and CI^{KO} permeabilized cells, calculated as the ratio of baseline CII respiration (without ADP) to H$^+$ leak.

(G) ATP synthesis contribution to CII respiration in vehicle and chronic Rot-treated, as well as in WT and CI^{KO} permeabilized cells, calculated as the ratio of coupled CII respiration (with ADP) to ATP synthesis.

(H) Oxygen consumption rates in WT, CI^{KD}, and CI^{KO} permeabilized cells respiring on Succ + Rot + ADP in the absence or presence of cyt c. *p* values represent one-way ANOVA analysis.

(I) Calibrated TMRM signal in WT, CI^{KD}, and CI^{KO} permeabilized cells respiring on Succ + Rot + ADP in the absence or presence of cyt c. *p* values represent one-way ANOVA analysis.

(legend continued on next page)

(J) Quantification of respiratory rates of WT vs. CI^{KD} (n = 4), WT vs. CI^{KO} (n = 7), and $NDUFS4^{WT}$ (whole CI) and $NDUFS4^{KO}$ (P-module) (n = 4) permeabilized cells respiring on CIV substrates. p values represent t test analysis.
(K) Calibrated TMRM signal in WT vs. CI^{KD} (n = 4), WT vs. CI^{KO} (n = 7), and $NDUFS4^{WT}$ vs. $NDUFS4^{KO}$ (n = 4) permeabilized cells respiring on CIV substrates. p values represent t test analysis.
Violin plots show dots representing every replicate and a dotted line indicating the mean of all experiments.

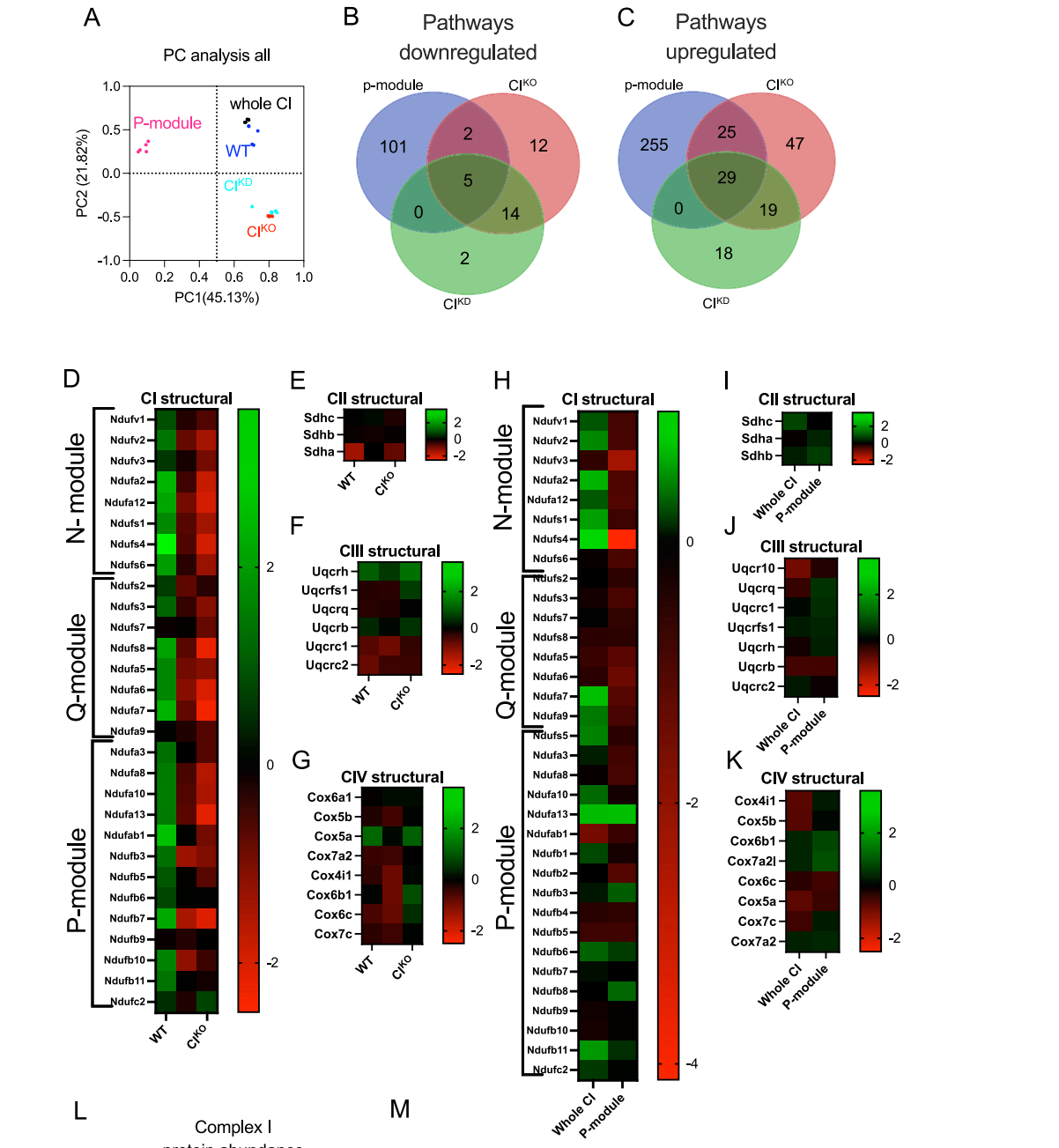

(legend on next page)

Figure S5. Proteomics analysis of WT, CI^{KD}, CI^{KO}, $NDUFS4^{WT}$ (whole CI), and $NDUFS4^{KO}$ (P-module) isolated mitochondria, related to Figure 3

(A) Principal component analysis using the whole quantified protein dataset.

(B and C) Venn diagrams comparing the Gene Ontology pathways significantly downregulated (B) or upregulated (C) estimated by gene set enrichment analysis (GSEA).

(D–K) Mean relative protein abundances of (D) CI subunits in WT, CI^{KD}, and CI^{KO} mitochondria; (E) CII subunits in WT, CI^{KO}, and CI^{KO} mitochondria; (F) CIII subunits in WT, CI^{KD}, and CI^{KO} mitochondria; (G) CIV subunits in WT, CI^{KD}, and CI^{KO} mitochondria; (H) of CI subunits in $NDUFS4^{WT}$ and $NDUFS4^{KO}$ mitochondria; (I) of CII subunits in $NDUFS4^{WT}$ (whole CI) and $NDUFS4^{KO}$ (P-module)mitochondria; (J) of CIII subunits in $NDUFS4^{WT}$ (whole CI) and $NDUFS4^{KO}$ (P-module) mitochondria; and (K) of CIV subunits in $NDUFS4^{WT}$ (whole CI) and $NDUFS4^{KO}$ (P-module)mitochondria.

(L) Relative quantitative change in abundance of the structural subunits detected for the indicated CI module between WT and $NDUFS4^{KO}$ mitochondria of the proteins shown in (H). Plots show dots representing every replicate, the mean, and standard deviation of all experiments. Asterisks represent t test analysis, ***p value < 0.001, *p value < 0.05.

(M) Volcano plot analysis showing relative abundance changes of all mitochondrial proteins detected in WT vs. CI^{KD}, in WT vs. CI^{KO}, and in $NDUFS4^{WT}$ (whole CI) and $NDUFS4^{KO}$ (P-module). n = 3 for all experiments.

Statistical significance of changes between groups was evaluated by Student's t test.

Labels in WT vs. CI^{KD}: (1) NDUFS4, (2) NDUFA7, (3) NDUFB3, (4) NDUFS6, (5) NDUFS2, (6) NDUFB11; (blue cross): NDUFAF8; (a) Timm44, (b) Fkbp10, (c) Acadm, (d) Dbi, (e) Dcxr, (group f) Acp6, Dbt, Mrpl33, D2hgdh, (g) Trap1, (h) Acad10, (i) Pitrm1, (j) Smim20, (k) Aldhl2, and (l) Acad1.

Labels in WT vs. CI^{KO}: (1) NDUFS4, (2) NDUFA7, (3) NDUFS8, (4) NDUFB7, (5) NDUFA12, (6) NDUFA2, (7) NDUFA13, (8) NDUFS6, (9) NDUFA8, (10) NDUFA10, (11) NDUFB5, (12) NDUFB11, (13) NDUFAB1; (blue cross): NDUFAF8; (a) Acot2, (b) Triap1, (c) Cisd3, (d) Mrpl12, (e) Acadm, (group f) Aldh9a1, Fxn, Acadl, Spire1, Fdps, Dld, Rdh13, Rot1, Tom34, Htaip2, Acap1, (g) Mul1, (group h) Gatd3a, Mmab, Rmdn3, Acadsb and Maoa.

Labels in whole vs. P-module: (1) NDUFS4, (2) NDUFB2, (3) NDUFB3; downregulated: Lylpa1, Agpa5, Prkaca, Clpp, Dld, Nsun2, Slc25a12, CoQ3, Mfn2; up-regulated: Dmac1, Slc25a15, Bcs1l, Ptrh1, Mrpl34, Auh, Timm13, Fastk, Timm22, Sdhb, Timm29, C2hgdh, Mrpl10, Mrps27, Slc25a11, Timm8a1, Dmac2, Hsd17b10, Tstd3, and Chchd4.

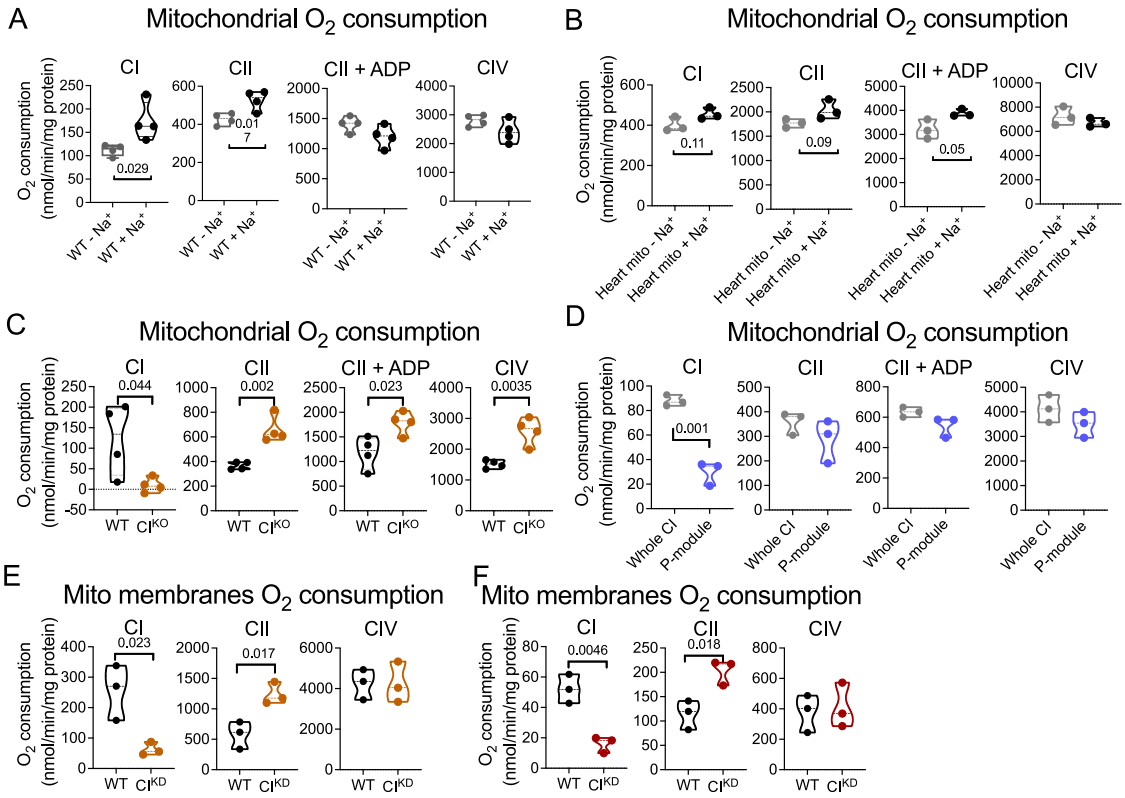

Figure S6. Quantification of mitochondrial O_2 consumption in different mitochondrial types and conditions, related to Figures 4 and 5

(A and B) Quantification of respiratory rates of (A) WT or (B) mouse heart mitochondria without and with Na^+ in the respiratory buffer oxidizing CI, CII, CII+ADP, and CIV substrates.

(C and D) Quantification of respiratory rates of (C) WT vs. $ND6^{KO}$ and (B) whole CI vs. P-module without Na^+ in the respiratory buffer oxidizing CI, CII, CII+ADP, and CIV substrates.

(E and F) Quantification of respiratory rates of (E) WT vs. $ND6^{KD}$ and (F) WT vs. $ND6^{KO}$ mitochondrial membranes oxidizing CI, CII, and CIV substrates. All quantifications were corrected by their respective specific inhibitor.

Violin plots show dots representing every replicate and a dotted line indicating the mean of all experiments. *p* values represent t test analyses.

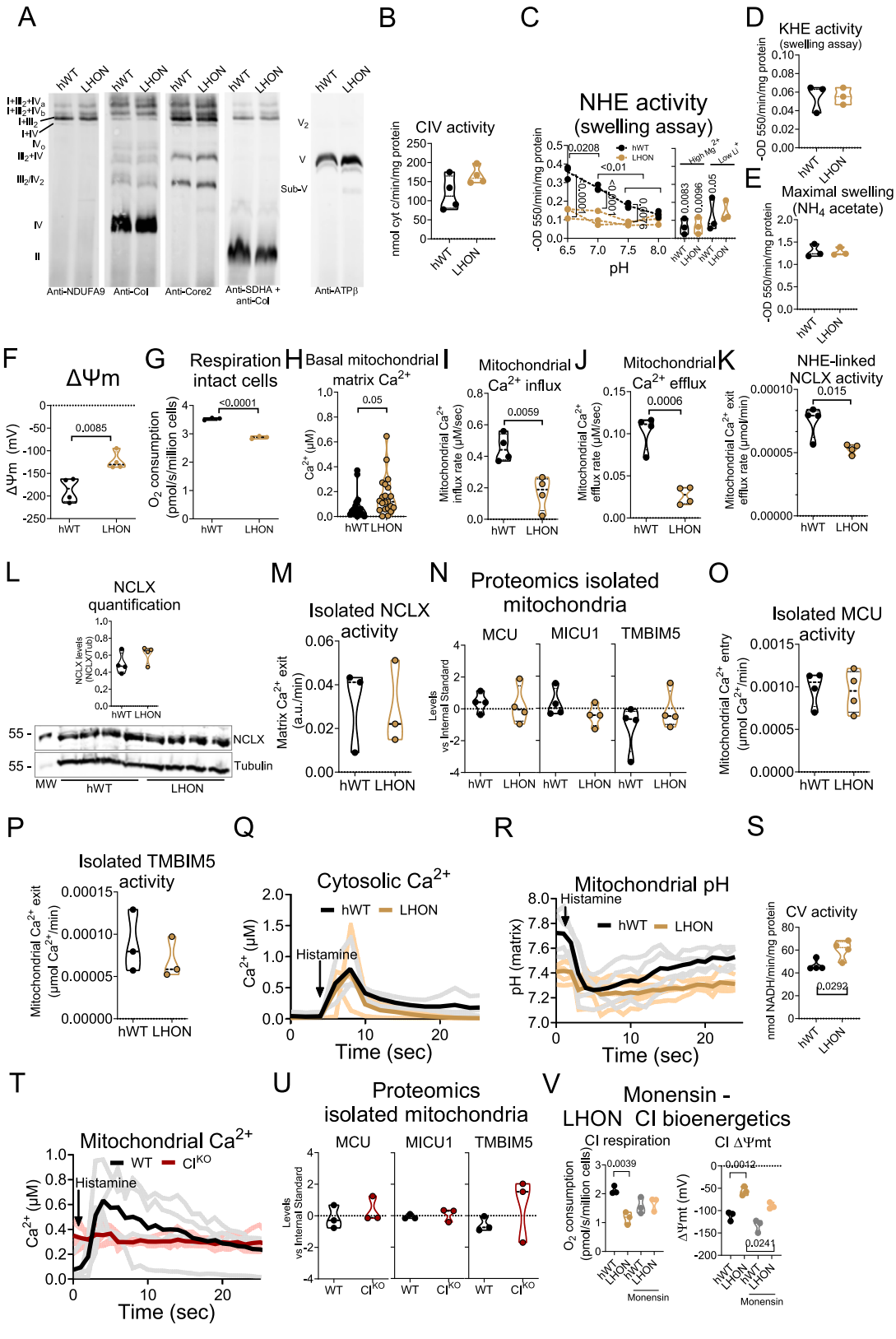

(legend on next page)

Figure S7. The specific defect of CI-NHE in LHON-causing m.11778 causes defects in Ca^{2+} management, related to Figure 7

(A) Blue-native electrophoresis (BN-PAGE) of mitochondria from hWT and LHON cybrid cell lines (n = 2) immunoblotted to detect subunits of CI (anti-NDUFA9), CIV (anti-CoI), CIII (anti-Core2), CII (anti-SDHA), and CV (anti-ATPβ).

(B) KCN-sensitive cyt c oxidation in mitochondrial membranes from hWT and LHON mitochondria (n = 4).

(C) Passive swelling reverse NHE activity in hWT and LHON was assessed in different buffer pHs and in the presence of 50 mM $MgCl_2$ or with 2 mM LiCl (n = 3). p values represent two-way ANOVA analysis among all conditions. p values in high Mg^{2+} and low Li^{+} are against hWT at their corresponding, same pH (i.e., pH 7).

(D) Passive KHE activity swelling assay in hWT and LHON intact mitochondria (n = 3).

(E) Maximal swelling assay in hWT and LHON intact mitochondria was performed in NH_4 acetate buffer (n = 3).

(F) Calibrated TMRM signal of hWT and LHON intact cells imaged by confocal microscopy (n = 4).

(G) Oxygen consumption in hWT and LHON intact cells (n = 3). p values represent a t test analysis.

(H) Basal mitochondrial Ca^{2+} levels were measured by confocal microscopy in hWT and LHON cells transfected with Cepia2mt (n = 18 in hWT and n = 21 in LHON). p values represent a t test analysis.

(I) Mitochondrial Ca^{2+} influx was calculated from the signals in Figure 4K (n = 4). p values represent a t test analysis.

(J) Mitochondrial Ca^{2+} efflux was calculated from the signals in Figure 4K (n = 4). p values represent a t test analysis.

(K) Mitochondrial Ca^{2+} efflux was evaluated in isolated mitochondria respiring on 10 mM succinate, 1 μM rotenone, and 4 mM ADP, reaching similar ΔΨmt values, loaded with a 50 μM bolus of $CaCl_2$ in the presence of Na^{+} and 10 μM calcium green (n = 4). p values represent a t test analysis.

(L) SDS-PAGE western blot showing the levels of NCLX and tubulin from whole hWT and LHON cell extracts (MW, molecular weight). Inset: ratio NCLX/tubulin of four independent biological replicates.

(M) Isolated NCLX activity was assessed in non-respiring mitochondria loaded with 10 μM Fluo4-AM after the addition of 50 μM $CaCl_2$ in the presence of Na^{+} (n = 3).

(N) Proteomic analysis showing the relative abundances of MCU, MICU2, and TMBIM5 relative to internal standard in hWT and LHON isolated mitochondria.

(O) Mitochondrial Ca^{2+} influx was evaluated in isolated mitochondria respiring on 10 mM succinate, 1 μM rotenone, and 4 mM ADP, reaching similar ΔΨmt values, loaded with a 50 μM bolus of $CaCl_2$ in the presence of Na^{+} and 10 μM calcium green (n = 4).

(P) Mitochondrial Ca^{2+} efflux was evaluated in isolated mitochondria respiring on 10 mM succinate, 1 μM rotenone, and 4 mM ADP loaded with a 50 μM bolus of $CaCl_2$ in the absence of Na^{+} and presence of 10 μM calcium green (n = 4).

(Q) Cytosolic Ca^{2+} levels measured by confocal microscopy of hWT and LHON cells transfected with cytoGECO before and after the addition of histamine. Each experiment is represented by semi-transparent lines and the mean by an opaque line.

(R) Mitochondrial pH levels measured by confocal microscopy of hWT and LHON cells transfected with mito-sypHer before and after the addition of histamine. Each experiment is represented by semi-transparent lines and the mean by an opaque line.

(S) Oligomycin (Olig)-sensitive ATPase activity in hWT and LHON mitochondrial membranes. p values represent t test analysis.

(T) Mitochondrial Ca^{2+} was measured with calibrated Cepia2mt in WT vs. CI^{KO} cells before and after stimulation with 100 μM histamine (n = 4 in WT and n = 5 in CI^{KO}).

(U) Proteomic analysis showing the relative abundances of MCU, MICU, and TMBIM5 relative to internal standard in WT and CI^{KO} isolated mitochondria.

(V) CI-dependent respiratory rates (left) and ΔΨmt (right) isolated mitochondria treated with vehicle or 50 nM monensin. p values represent a one-way ANOVA analysis.

Violin plots show dots representing every replicate and a dotted line indicating the mean of all experiments.